ATOM: A PRETRAINED NEURAL OPERATOR FOR MULTITASK MOLECULAR DYNAMICS

Anonymous authors
Paper under double-blind review

ABSTRACT

Molecular dynamics (MD) simulations underpin modern computational drug discovery, materials science, and biochemistry. Recent machine learning models provide high-fidelity MD predictions without the need to repeatedly solve quantum mechanical forces, enabling significant speedups over conventional pipelines. Yet many such methods typically enforce strict equivariance and rely on sequential rollouts, thus limiting their flexibility and simulation efficiency. They are also commonly single-task, trained on individual molecules and fixed timeframes, which restricts generalization to unseen compounds and extended timesteps. To address these issues, we propose Atomistic Transformer Operator for Molecules (ATOM), a pretrained transformer neural operator for multitask molecular dynamics. ATOM adopts a quasi-equivariant design that requires no explicit molecular graph and employs a temporal attention mechanism, enabling accurate parallel decoding of multiple future states. To support operator pretraining across chemicals and timescales, we curate TG80, a large, diverse, and numerically stable MD dataset with over 2.5 million femtoseconds of trajectories across 80 compounds. ATOM achieves state-of-the-art performance on established single-task benchmarks, such as MD17, RMD17 and MD22. After multitask pretraining on TG80, ATOM shows exceptional zero-shot generalization to unseen molecules across varying time horizons. We believe ATOM represents a significant step toward accurate, efficient, and transferable molecular dynamics models.

1 INTRODUCTION

Molecular dynamics (MD) serves as a computational microscope of atomic motion and is now integral to drug discovery and materials science pipelines (Dror et al., 2012; De Vivo et al., 2016). In ab initio molecular dynamics, quantum-mechanical density functional theory (DFT) is used to compute atomic forces, and the resulting equations of motion are integrated to generate high-fidelity trajectories. However, DFT's computational complexity scales at least cubically with the number of atoms, and relies on double-precision arithmetic that limits GPU acceleration (Kresse & Furthmüller, 1996; Stein et al., 2020; Li et al., 2024).

Neural approaches have recently emerged as a promising solution to the scalability bottleneck. *Equivariant* architectures, in particular, encode physical symmetries to model interatomic dynamics, achieving ab initio-level accuracy at significantly reduced computational cost (Batzner et al., 2022; Musaelian et al., 2022; Batatia et al., 2022; 2023; Xu et al., 2024). While equivariance is often deemed essential for improving generalization, strict symmetry preservation involves substantial tradeoffs (Xu et al., 2024; Schreiner et al., 2023). Architectures that enforce exact equivariance at every layer often increase computational overhead, restrict model expressivity, and complicate optimization (Fuchs et al., 2020; Brehmer et al., 2023; Elhag et al., 2025). It is unclear whether symmetry constraints can be relaxed without sacrificing accuracy for molecular dynamics.

Furthermore, most existing methods for molecular dynamics are *autoregressive*, predicting the next state based on the current one (Köhler et al., 2019; Fuchs et al., 2020; Thiemann et al., 2025). Autoregressive approaches often struggle to capture long-horizon temporal dependencies and accumulate error as the prediction horizon grows (Bengio et al., 2015; Bergsma et al., 2023; Taieb & Atiya, 2016). Inference speeds are also constrained by the need for sequential integration, failing to exploit modern, highly parallel compute architectures. One exception is Equivariant Graph Neural

Operator (EGNO) (Xu et al., 2024), which models the entire trajectory with neural operator learning. Nevertheless, EGNO enforces strict equivariance and is single-task in nature, i.e., it is trained and evaluated on trajectories of each molecule separately with a fixed time horizon, which limits *zero-shot generalization* to unseen molecules or timeframes.

Our Main Contributions. In this work, we address the above issues regarding equivariance, autoregression, and zero-shot generalization within a unified framework, which we call *Atomistic Transformer Operator for Molecules (ATOM)*. To this end, we propose a pre-trained neural operator with a transformer backbone for molecular dynamics and introduce a new MD dataset, TG80, which is both chemically diverse and numerically stable for multitask pretraining and benchmarking.

- *Design innovations*. ATOM is *quasi-equivariant* by employing an equivariant lifting layer that produces symmetry-aware features, while allowing subsequent transformer blocks to be unconstrained for flexibility and expressiveness. Unlike autoregressive models, ATOM allows *parallel decoding* of molecule states across multiple timesteps, directly learning the trajectory operator. By encoding time lags via a novel temporal rotary position embedding, ATOM enhances temporal interpolation and extrapolation, enabling robust predictions across multiple time horizons. Finally, ATOM requires no predefined molecular graph and operates directly on *point clouds*, naturally accommodating long-range spatial interactions without the need for hand-crafted connectivity.
- *Performance highlights*. ATOM sets new state-of-the-art on single-task MD benchmarks. For larger, sparsely connected molecules in MD22, ATOM significantly outperforms existing graph-based baselines by capturing the long-range atomic interactions. In the multitask regime, we pretrain ATOM on TG80 trajectories from multiple molecules and varying timeframes, demonstrating significant zero-shot transfer to both unseen molecules and timesteps, improving existing baselines by 39.75% on average. This achieves performance on par with existing specialized baselines tailored for such molecules and timeframes. To the best of our knowledge, this is the first method that demonstrates such generalization capability in molecular dynamics.

We believe our work represents a shift in molecular dynamics modeling, where we demonstrate the potential of quasi-equivariance designs and zero-shot generalization to out-of-domain systems, which is enabled by the comprehensive TG80 MD dataset.

2 RELATED WORK

Equivariant Neural Networks. Equivariance (to transformations such as rotation, reflection, and translation) has emerged as an essential physics-informed prior for deep learning models on molecular data (Bronstein et al., 2021; Duval et al., 2023). Early works employed convolutional approaches to achieve translation equivariance in E(3) (Weiler et al., 2018; Wu et al., 2020) or tensor product attention and spherical harmonics to enforce roto-translational equivariance in SE(3) (Fuchs et al., 2020; Thomas et al., 2018). In contrast, message passing neural network (MPNN) frameworks, such as Equivariant Graph Neural Network (EGNN) and others (Garcia Satorras et al., 2021; Gasteiger et al., 2021; Huang et al., 2022), achieve equivariance by operating on strictly equivariant features, such as inter-node distances and directions. While effective, MPNNs typically assume a fixed molecular graph. This is problematic when the underlying structure contains non-local interactions and dynamic bonding effects (e.g., resonances, transient interactions), which render predefined graphs inaccurate over time (Knutson et al., 2022; Luo et al., 2021). To address this issue, we model molecules as point clouds, with our attention represented as a fully connected graph that allows unrestricted information propagation across the molecule.

Time-coarsened Molecular Dynamics Time coarsening is a coarse-graining method which preserves molecular structure, but compresses many short integration steps into a few large-stride updates to reduce the cost of long-time simulation (Kmiecik et al., 2016). Stochastic coarse-graining approaches often learn transition kernels on configuration space, bypassing explicit integration of the equations of motion. Klein et al. (2023) learns such a kernel with a normalizing flow and uses it as an MCMC proposal targeting the Boltzmann distribution, Hsu et al. (2024) uses a conditional diffusion model to learn a transition probability matrix, and Yu et al. (2025) uses flow-matching to learn a vector field transporting current states to future states. Closer to our framework, deterministic methods such as MDNet (Zheng et al., 2021) and TrajCast (Thiemann et al., 2025) learn a GNN and EGNN, respectively, which autoregressively predict fixed strides 10-100 times larger than those of MD integrators. Bigi et al. (2025) incorporates Hamiltonian structure and explicit energy-conservation. Most of the methods require direct force learning and are sequential in nature, while ATOM may be interpreted as a *force-free* deterministic coarse-graining approach, wherein temporal pushforward is approximated by a learned propagation operator which is decoded *in parallel*.

Neural Operators. Neural operators are deep learning methods for learning operators between function spaces (Kovachki et al., 2021). A wide variety of architectures have been proposed for such operator learning. Notably, Fourier Neural Operator (FNO) (Li et al., 2021) learns an operator in the Fourier domain, while its derivatives G-FNO (Helwig et al., 2023) and PINO (Li et al., 2023b), respectively, add group equivariance and physics-informed properties. Xu et al. (2024) bridges this framework with molecular dynamics by recasting the task as learning a propagation operator that evolves historical atomic positions into their future configurations. Specifically, EGNO (Xu et al., 2024) is proposed by integrating EGNN and FNO layers to learn dynamic trajectories, capturing both spatial and temporal correlations. Recently, transformer neural operators (Bryutkin et al., 2024; Hao et al., 2023; Li et al., 2023a) have surpassed the performance of FNO in most partial differential equation (PDE) tasks. Notably, OFormer (Li et al., 2023a) uses a linear Galerkin-type attention mechanism, which omits the softmax and instead interprets the latent column vectors as basis functions. General Neural Operator Transformer (GNOT) (Hao et al., 2023) employs a novel subquadratic cross-attention methodology to integrate multiple feature types (e.g., shape and point relationships) into their transformer blocks. With ATOM, we unify the MD problem formulation and temporal discretization approach introduced by EGNO with the increased representational power of transformers in operator settings.

MD Benchmarks. Research on graph machine learning for molecular dynamics suffers from poor benchmarking (Bechler-Speicher et al., 2025). For example, despite the fact that MD17 Benzene exhibits non-physical noise approximately 1000 times higher compared to other compounds (Christensen & von Lilienfeld, 2020), it is still regularly employed to benchmark new models (Bihani et al., 2023; Huang et al., 2022; Liao & Smidt, 2023; Xu et al., 2024). The practical relevance of single-task learning on these datasets is also dubious, as predicting trajectories for molecules with existing numerical solutions offers minimal benefit. We believe the strengths of neural approaches emerge in transfer learning, where models generalize to unseen compounds, thereby circumventing the computational costs associated with explicit numerical simulations. This motivates our development of TG80 to facilitate multitask dynamics learning across molecular systems.

3 ATOMISTIC TRANSFORMER OPERATOR FOR MOLECULES (ATOM)

In this section, we first introduce the problem formulation (Section 3.1) and then propose the framework of ATOM by introducing the key model and training designs (Section 3.2). We then discuss the multitask pretraining for ATOM and introduce TG80 MD dataset (Section 3.3).

3.1 PROBLEM FORMULATION

We follow (Xu et al., 2024) to cast molecular dynamics prediction as operator learning. We model a molecule of N atoms as a point cloud in $\mathbb{R}^3$, which we denote as $\mathcal{G}^{(t)}$ for a given system state time t. In particular, we write $\mathcal{G}^{(t)} = (\mathbf{x}_i^{(t)}, \mathbf{v}_i^{(t)})_{i=1}^N$ that represent molecules in terms of the atom positions $\mathbf{x}$ and velocities $\mathbf{v}$. Our objective is to predict a future trajectory $\mathcal{G}^{(t+\Delta t)}$, where $\Delta t \in [0, \Delta T]$.

Similar to (Xu et al., 2024), we focus on predicting the position states only. Let $\mathcal{U}\colon [0, \Delta T] \to \mathbb{R}^{N\times 3}$ be the trajectory function mapping Δt to $U(\Delta t) \in \mathbb{R}^{N\times 3}$ representing molecule positions Δt in the future. We assume a solution operator $F^\dagger\colon \mathcal{G}^{(t)} \to \mathcal{U}$ exists which provides the underlying future trajectory given system states at t. Thus, the goal of molecular dynamics prediction becomes training a neural operator $F_\theta(\mathcal{G}^{(t)})$ to approximate the target trajectory function $F^\dagger(\mathcal{G}^{(t)})$: $\min_\theta \mathbb{E}_{\mathcal{G}^{(t)}} \mathcal{L}\big(F_\theta(\mathcal{G}^{(t)})(t), F^\dagger(\mathcal{G}^{(t)})(t)\big)$, for some loss function $\mathcal{L}\colon \mathcal{U}\times\mathcal{U} \to \mathbb{R}$. Here, expectation is with respect to the different initial states. By discretizing over the temporal domain and considering L_2 loss, we optimize the neural operator with a discretized temporal sampling of the states:

$$\min_\theta \frac{1}{P}\sum_{p=1}^{P} \mathbb{E}_{\mathcal{G}^{(t)}} \left\| F_\theta\left(\mathcal{G}^{(t)}\right)(\Delta t_p) - F^\dagger\left(\mathcal{G}^{(t)}\right)(\Delta t_p)\right\|_2^2. \tag{1}$$

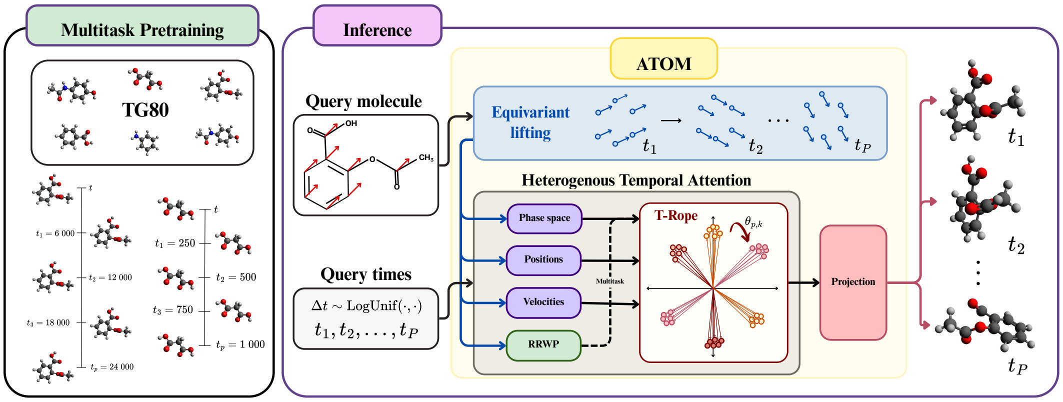

Figure 1: **ATOM Pipeline**. We pretrain ATOM on the TG80 dataset across multiple molecules with stochastic time lags. At inference, ATOM takes a query molecule and timestamps and directly outputs corresponding molecular states.

where $\{\Delta t_1, ..., \Delta t_p\}$ are discrete timesteps. We replace the true future state $F^\dagger(\mathcal{G}^{(t)})(\Delta t_p)$ with the known future ground truth node positions $\mathbf{x}^{(t+\Delta t_p)}$ for $\Delta t_p \in [0, \Delta T]$.

Quasi-equivariance. We formally define quasi-equivariance, motivated by (Elhag et al., 2025).

Definition 3.1 (ε-quasi-equivariance). *We call a function $f : \mathcal{X} \to \mathcal{Y}$, ε-quasi-equivariant with respect to group G if it satisfies $\mathbb{E}_{x\in\mathcal{X}} \| \int_G f(\phi(g)(x))d\mu(g) - \int_G \rho(g)(f(x))d\mu(g)\| \leq \varepsilon$, where μ denotes the normalized Haar measure.*

In practice, we approximate the group integration with Monte Carlo samples from G.

Single- and multitask. Unlike prior works (Schreiner et al., 2023; Xu et al., 2024), we consider both single-task and multitask settings. *Single-task* refers to the case where a separate model is independently trained and evaluated on each molecule and fixed timeframes. This corresponds to the conventional practice in molecular dynamics benchmarks. *Multitask* instead pretrains one unified model on several molecules across varying time lags and evaluates out-of-domain trajectories on unseen molecules, thereby directly testing zero-shot cross-molecule generalization. Under a multitask setting, the objective (1) computes the expectation over trajectories of multiple molecules.

3.2 ATOM MODEL AND TRAINING DESIGN

Here we outline the pipeline of ATOM. At its core is an *equivariant lifting* layer (Section 3.2.1), which maps atomic positions, velocities and their phase features into a richer embedding space while preserving symmetry under the Euclidean group $E(3)$. The lifted embeddings are then processed by the ATOM attention block, which applies *heterogeneous attention* over positions, velocities, and phase features with chemical augmentation (Section 3.2.2). To capture temporal dynamics, we incorporate a *temporal rotary position embedding* (T-RoPE) (Section 3.2.2) that depends only on time lags and is shared across atoms, ensuring translation invariance in time and permutation invariance within each molecule. The parameterized ATOM can be written by

$$F_\theta := \mathcal{P} \circ \sigma(\mathcal{K}_L) \circ \cdots \circ \sigma(\mathcal{K}_1) \circ \mathcal{Q}$$

where $\mathcal{Q}$, $\mathcal{P}$ denotes the equivariant lifting and projection operators respectively. $\mathcal{K}_l, l = 1, ..., L$ are the data-dependent kernels induced by cross attention (See Appendix G.1), and σ denotes some nonlinear activation function.

Finally, to counter numerical noise in training trajectories, we inject randomly sampled position and velocity perturbations during training (Section 3.2.3), which improves robustness and acts as a regularizer against overfitting. The overall pipeline of ATOM is in Figure 1.

3.2.1 $E(3)$ EQUIVARIANT LIFTING

To model atomic states in a symmetry-respecting way, each atom is encoded with its 3D position and velocity, augmented with their norms: $\mathbf{x} = (x, y, z, \sqrt{x^2+y^2+z^2})$, $\mathbf{v} = (v_x, v_y, v_z, \sqrt{v_x^2+v_y^2+v_z^2})$. To construct higher-dimensional features that remain consistent with $E(3)$ symmetry, we apply *equivariant lifting* that maps the inputs through learnable functions that preserve group actions. Specifically, we use $E(3)$-equivariant linear layers (Geiger & Smidt, 2022) that lifts the position and velocity vectors to a feature space. The resulting features satisfy the equivariance constraints by construction. We further construct phase space of each atom by augmenting the position and velocity vectors with atomic number, which is subsequently processed by a learnable equivariant layer to obtain a lifted representation. The final lifted embedding for a molecule is given by $(\mathbf{X}, \mathbf{V}, \mathbf{Z}) \in \mathbb{R}^{3\times NP\times d_v}$ corresponding to position, velocity and phase features. The second dimension aggregates nodes and time for attention and d_v is the embedding space dimension.

We highlight that after the equivariant lifting layer, we do not enforce equivariance in the subsequent Transformer blocks. This relaxation leads to improved performance compared to fully equivariant designs and, show robustness to random rotations of the trajectories compared to non-equivariant baselines (see Section 4.4).

3.2.2 ATOM HETEROGENEOUS TEMPORAL ATTENTION

We employ a heterogeneous temporal attention mechanism to enable mixing between multiple features $(\mathbf{X}, \mathbf{V}, \mathbf{Z}) \in \mathbb{R}^{3\times NP\times d_v}$ across spatial and temporal dimensions. We use the phase space embedding $\mathbf{Z}$ as the query and attend to the key-value pairs formed from all features $\mathbf{X}, \mathbf{V}, \mathbf{Z} \in \mathbb{R}^{NP\times d_v}$. In Figure 5, we show that this improves performance by 6.36% over standard self-attention for single-task prediction. In addition, to encode temporal information, we introduce Temporal RoPE (T-RoPE), an adaptation of RoPE (Su et al., 2023) to irregular time lags by driving the phases with timestamps built from per-step increments $\{\Delta t\}$.

Let the hidden dimension per head be d_h (even). We define frequencies $\omega_k = b^{-2k/d_h}$ for $k = 0, \ldots, d_h/2-1$. Given per-step time increments $\{\Delta t_p\}_{p=1}^{P}$, we build timestamps $t_p = t + \sum_{r=1}^{p} \Delta t_r$, and assign a *single* rotation to all N atoms at timestep p: $\mathbf{R}_p = \operatorname{diag}\big(\mathbf{R}(\theta_{p,0}), \ldots, \mathbf{R}(\theta_{p,d_h/2-1})\big) \in \mathbb{R}^{d_h\times d_h}$, where $\theta_{p,k} = \frac{\omega_k}{\tau}\big(t_p - t_0\big)$ and $\mathbf{R}(\theta) \in \mathbb{R}^{2\times 2}$ is the rotation matrix with angle θ and $\tau > 0$ is a timescale hyperparameter. Suppose the query molecule state at time p is given as $\mathbf{Q}_p \in \mathbb{R}^{N\times d_h}$ and key molecule state at time p' is $\mathbf{K}_{p'} \in \mathbb{R}^{N\times d_h}$. We apply $\mathbf{R}_p, \mathbf{R}_{p'}$ to $\mathbf{Q}_p, \mathbf{K}_{p'}$ respectively so that the rotary dot product $\mathbf{Q}_p\mathbf{R}_p(\mathbf{K}_{p'}\mathbf{R}_{p'})^\top$ depends only on the time interval $t_{p'} - t_p$. This makes attention *translation invariant* in time, which allows for interpolation and extrapolation across irregular increments $\{\Delta t_p\}$. In addition, sharing the same $\mathbf{R}_p$ across all N atoms in a molecule ensures *permutation-invariance* within a timestep. For aggregated query and key matrices $\mathbf{Q}, \mathbf{K} \in \mathbb{R}^{NP\times d_h}$, we denote the application of temporal Rotary Position Embedding (RoPE) across P timesteps and N atoms as $\text{T-RoPE}(\mathbf{Q}), \text{T-RoPE}(\mathbf{K}) \in \mathbb{R}^{NP\times d_h}$.

Specifically, a single-head attention layer of ATOM computes

$$\sum_{\mathbf{F}\in\{\mathbf{X},\mathbf{V},\mathbf{Z}\}} \gamma_{\mathbf{F}} \operatorname{softmax}\left(\frac{\text{T-RoPE}(Q(\mathbf{Z}))\ \text{T-RoPE}(K(\mathbf{F}))^\top}{\sqrt{d_h}}\right) V(\mathbf{F}),$$

where $Q(\cdot), K(\cdot), V(\cdot)$ represent the query, key and value projections. We introduce learnable weights $\gamma_{\mathbf{F}}$ to modulate the relative importance of each feature. In Appendix G.1, we show that heterogeneous attention is equivalent to a kernel integral operator and discuss its properties.

3.2.3 TRAINING WITH LABEL NOISE REGULARIZATION

Many DFT datasets are inherently noisy (Christensen & von Lilienfeld, 2020), and MD models can overfit to this noise. Motivated by the regularization effect of label noise (Damian et al., 2021; HaoChen et al., 2020), we augment the observed node positions $\mathbf{x}$ and velocities $\mathbf{v}$ by random Gaussian noise $\boldsymbol{\xi}_{\mathbf{x}}, \boldsymbol{\xi}_{\mathbf{v}} \sim \mathcal{N}(\mathbf{0}, \sigma^2\mathbf{I})$ during training. Let $\mathcal{G}_{\boldsymbol{\xi}}^{(t)} = (\mathbf{x}_i^{(t)} + \boldsymbol{\xi}_{x,i}, \mathbf{v}^{(t)} + \boldsymbol{\xi}_{v,i})$ be the noised initial state at time t. We minimize the following regularized loss

$$\min_{\theta} \frac{1}{P} \sum_{p=1}^{P} \mathbb{E}_{\mathcal{G}^{(t)}, \boldsymbol{\xi}, \boldsymbol{\xi}_x^p} \left\| F_\theta \left(\mathcal{G}_{\boldsymbol{\xi}}^{(t)} \right) (\Delta t_p) - \left(\mathbf{x}^{(t+\Delta t_p)} + \boldsymbol{\xi}_x^p \right) \right\|_2^2 .$$

A similar strategy has also appeared in graph neural network (GNN)-based MD models and neural operator pretraining (Dauparas et al., 2022; Zhou et al., 2024a; Hao et al., 2024). We only apply noise augmentation during training and evaluate on the unperturbed ground-truth trajectories.

Comparison to EGNO. We highlight that ATOM adopts fundamentally different design choices compared to EGNO. First, EGNO is a graph EGNN operating on fixed bond connectivity, whereas ATOM uses an E(3)-equivariant lifting layer followed by globally connected point-cloud attention, which better handles long-range and sparsely bonded interactions. Second, EGNO is strictly equivariant end-to-end, while ATOM is quasi-equivariant, enforcing equivariance only in the lifting stage and relaxing it in deeper transformer layers, which our ablations show improves accuracy. Third, EGNO models time via Fourier temporal convolution, whereas ATOM uses Temporal RoPE, allowing translation-invariant handling of irregular time gaps and stronger temporal extrapolation. T-RoPE also uniquely allows modifying the time-horizon ΔT *at inference* by modulating the rotary phases (Section 3.2.2). Consequently, a pretrained ATOM can be evaluated at arbitrary ΔT values without retraining.

3.3 MULTITASK ATOM PRETRAINING AND TG80 DATASET

This section adapts ATOM for the multitask setting, where the aim is to predict future trajectories for unseen molecules. In order to more effectively distinguish molecules, we construct a radius graph of 1.6 Å based on atomic positions, and apply *random walk positional encoding* (Ma et al., 2023; Lobato et al., 2021) to augment the phase vector $\mathbf{z}$. We describe the process in detail in Appendix D.2 and highlight that such a graph depends only on atomic positions, not chemical bonds.

During multitask training, each mini-batch contains trajectories from multiple molecules. In addition, we perform random sampling for the time lags Δt from a log-uniform distribution between Δt_{min} and ΔT, namely $\Delta t \sim \text{LogUnif}(\Delta t_{\text{min}}, \Delta T)$. This aims to enhance the robustness of interpolation and extrapolation in the temporal domain, a consideration that has been similarly explored in (Schreiner et al., 2023). Let $\mathcal{M}$ denote the set of training molecules and let $\mathcal{G}_m^{(t)}$ represent the state of molecule $m \in \mathcal{M}$ at timestamp t. We can write the pretraining multitask objective as

$$\min_{\theta} \frac{1}{|\mathcal{M}|} \sum_{m \in \mathcal{M}} \mathbb{E}_{\mathcal{G}_m^{(t)},\, \Delta t \sim \text{LogUnif}(\Delta t_{\text{min}},\, \Delta T)} \left\| F_\theta \left(\mathcal{G}_m^{(t)}, \Delta t \right) (\Delta t) - \mathbf{x}_m^{(t+\Delta t)} \right\|_2^2 ,$$

where we take expectation with respect to initial states of multiple molecules in the training set, as well as the time lags. Here, we emphasize ATOM also takes a time lag, Δt, as input.

TG80 Dataset. To facilitate pretraining of our neural operator, we introduce **TG80**, a superset of the MD17 dataset. The initial seed set comprises 40 molecules: 8 MD17 compounds and 32 additional drug-like molecules selected through expert review. We then augment the seed molecules with structurally similar molecules from the PubChem dataset of 173 million compounds (Bolton et al., 2011). Accepted candidates had an ECFP-4 Tanimoto similarity between 0.875 and 0.925 to at least one seed molecule, and no more than 0.80 similarity to previously accepted molecules, alongside other criteria detailed in Appendix C.4 (Landrum et al., 2025; Rogers & Hahn, 2010; Rogers & Tanimoto, 1960). These thresholds follow common practice in the literature, balancing diversity while avoiding collapse into overly narrow chemical subspaces (Matter, 1997; Menke et al., 2021; Eastman et al., 2023; Harper et al., 2004; Zhang et al., 2023).

We generate all trajectories using ORCA V6.01 (Neese, 2022) with the PBE functional (Perdew et al., 1996), def2-SVP basis set (Weigend & Ahlrichs, 2005), Δ4 dispersion corrections (Caldeweyher et al., 2019; 2020; Wittmann et al., 2024) at one femtosecond resolution, 300K temperature, in vacuum. This resembles an enhanced RMD17, with more modern dispersion corrections to improve stability and allow for a larger step size (Christensen & von Lilienfeld, 2020). As a result, TG80 exhibits *more diverse dynamics* and *improved numerical stability*, with no compound exceeding 50 Å center-of-mass drift in Figure 8[1].

---

[1] Simulations ran on 32 AMD EPYC 7543 cores with 256 GB RAM per molecule, totalling 806,400 CPU-hours (quoted market cost USD 150 000).

4 EXPERIMENT RESULTS

Metrics. We use *State-to-trajectory* (S2T) and *state-to-state* (S2S) error to evaluate ATOM (Xu et al., 2024). Specifically, S2T $= \frac{1}{P}\sum_{p=1}^{P} \|\hat{\mathbf{x}}_p - \mathbf{x}_p\|_2^2$, measures the average discrepancy between the predicted $\hat{\mathbf{x}}$ and ground-truth positions $\mathbf{x}$ across entire trajectories, while S2S $= \|\hat{\mathbf{x}}_P - \mathbf{x}_P\|_2^2$, quantifies the error at the final predicted timestep.

Baselines. For comparison, we include a range of classic to state-of-the-art baselines, including Radial Field (RF) (Köhler et al., 2019), Tensor Field Networks (TFN) (Thomas et al., 2018), SE(3) Transformer (SE(3)-Tr.) (Fuchs et al., 2020), E(n) equivariant graph neural networks (EGNN) (Garcia Satorras et al., 2021), and EGNO (Xu et al., 2024). Our EGNN baselines are EGNN-Rollout (EGNN-R), which predicts timesteps autoregressively, and EGNN-Sequential (EGNN-S), which uses the output of each GNN as the prediction of a given frame. We set all baseline hyperparameters following previous works (Xu et al., 2024; 2022; Shi et al., 2021) and tune ATOM and EGNO hyperparameters as in Table 20 and Table 21.

Training setups. For training of ATOM and EGNO, we consider two temporal discretization strategies in selecting the timestamps $t_p = t + \sum_{r=1}^{p} \Delta t_r$: (1) *Uniform discretization* selects $t_p = t + p/P\Delta T$ and (2) *Tail discretization* selects $t_p = t + \overline{\Delta} + p/P(\Delta T - \overline{\Delta})$ for a lag $\overline{\Delta} \in [0, \Delta T]$. In the main paper, we present experiment results with uniform discretization and include the results with tail discretization in Appendix E. We perform early stopping on the lowest S2S validation loss checkpoint and report results as mean $\pm 2\sigma$ over *three training runs*. All experiments are run on an NVIDIA® RTX 5080 with wall-clock time and FLOP utilization detailed in Table 16.

4.1 SINGLE-TASK LEARNING

We benchmark on the MD17, RMD17, and MD22 DFT MD trajectory datasets (Chmiela et al., 2017; Christensen & von Lilienfeld, 2020; Chmiela et al., 2023). We partition the trajectories into train/validation/test splits of sizes 500/2000/2000, set $\Delta T = 3000$ fs and $P = 8$, and train for 2500 epochs following (Xu et al., 2024). For the performance on MD17 (Table 1), we directly quote the results from (Xu et al., 2024) except for EGNO. We design ATOM to have six transformer blocks with a hidden size of 256.

MD17 and RMD17. As shown in Table 1, ATOM compares favorably with state-of-the-art (SOTA) baselines on MD17 dataset, yielding average reductions of 14.96% (S2S mean squared error (MSE)) and 8.3% (S2T MSE) on average[2]. In Table 9 (Appendix E.1), we benchmark ATOM on RMD17, and observe similarly competitive performance against EGNO.

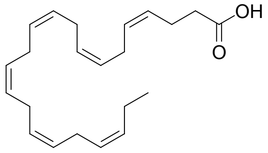

Figure 2: Docosahexaenoic acid (DHA)

MD22. To evaluate performance on larger molecules, we consider Ac-Ala3-NHMe (20 heavy atoms), docosahexaenoic acid (DHA with 24 heavy atoms), and stachyose (45 heavy atoms) from the MD22 dataset (Chmiela et al., 2023). ATOM remains competitive on these systems; whereas EGNO fails to converge (Table 2). We attribute this discrepancy to differing inductive biases: GNNs such as EGNO restrict message passing to a predefined bond or radius graph and can therefore under-represent long-range, non-bonded steric and electrostatic interactions that dominate the behavior of large, sparsely connected molecules (Alon & Yahav, 2021; Kosmala et al., 2023). This explains the poor performance of EGNO on MD22, which contains prototypically sparse molecules such as DHA, shown in Figure 2 (Nv et al., 2003). We further disentangle the role of connectivity from the use of attention by training a variant, ATOM-Graph attention network v2 (GATv2), in which our heterogeneous temporal attention is replaced by GATv2 layers (Brody et al., 2022) operating on the same bond/radius graph as EGNO. ATOM-GATv2 still substantially underperforms the full ATOM model, indicating that the performance gains stem from the fully connected point-cloud interaction pattern rather than from attention alone.

---

[2] We exclude benzene from the table due to the previously discussed high numerical noise.

Table 1: Single-task MSE ($\times 10^{-2}$) on MD17. Upper part: S2S MSE. Lower part: S2T MSE.

	Aspirin	Ethanol	Malonaldehyde	Naphthalene	Salicylic	Toluene	Uracil
RF	10.94±0.02	4.64±0.02	13.93±0.06	0.50±0.02	1.23±0.04	10.93±0.08	0.64±0.02
TFN	12.37±0.36	4.81±0.08	13.62±0.16	0.49±0.02	1.03±0.04	10.89±0.02	0.84±0.04
SE(3)-Tr.	11.12±0.12	4.74±0.02	13.89±0.04	0.52±0.02	1.13±0.04	10.88±0.12	0.79±0.04
EGNN	14.41±0.30	4.64±0.04	13.64±0.02	0.47±0.04	1.02±0.04	11.78±0.14	0.64±0.02
EGNN-R	9.96±0.14	4.61±0.01	13.04±0.03	0.44±0.05	0.96±0.01	10.19±0.15	1.11±0.04
EGNN-S	10.25±0.09	4.61±0.01	13.06±0.01	0.53±0.01	1.06±0.05	10.83±0.09	0.62±0.01
EGNO	9.64±0.15	4.57±0.01	**12.92**±0.00	**0.39**±0.00	0.89±0.01	11.00±0.00	**0.58**±0.02
MACE	6.95 ±0.00	2.06 ±0.00	17.99 ±0.26	0.72 ±0.00	1.05 ±0.00	6.44 ±0.00	0.75 ±0.00
ATOM	**6.82**±0.06	**3.52**±0.04	14.72±0.01	0.50±0.00	**0.88**±0.01	**4.66**±0.21	0.63±0.00
EGNN-R	7.35±0.19	3.21±0.00	**10.75**±0.04	**0.34**±0.06	1.09±0.12	4.53±0.08	0.89±0.02
EGNN-S	9.01±0.34	3.21±0.00	11.20±0.03	0.42±0.01	1.41±0.00	4.86±0.04	0.65±0.01
EGNO	9.64±0.15	4.57±0.01	12.92±0.00	0.39±0.00	0.90±0.01	10.99±0.00	**0.58**±0.02
MACE	5.06 ±0.00	2.84 ±0.00	16.09 ±0.03	0.57 ±0.00	0.55 ±0.00	3.26 ±0.00	1.08 ±0.00
ATOM	**5.62**±0.05	**2.62**±0.04	12.49±0.01	0.43±0.00	**0.86**±0.01	**2.27**±0.10	0.61±0.00

Table 2: Single-task MSE ($\times 10^{-2}$) on MD22. Upper: S2S. Lower: S2T

	Ac-Ala3-NHME	**DHA**	**Stachyose**
EGNO	357.89±3.94	178.39±4.91	42.11±0.10
ATOM-GATv2	223.57±0.66	16.72±0.44	41.40±0.37
ATOM	**9.65**±0.75	**10.60**±1.11	**21.25**±4.20
Gap	+97.30%	+94.06%	+49.54%
EGNO	232.40±6.75	116.45±3.34	30.84±0.03
ATOM-GATv2	113.26±0.04	14.39±0.32	29.70±0.15
ATOM	**7.55**±0.42	**9.66**±1.16	**18.13**±3.78
Gap	+96.75%	+91.70%	+41.22%

Table 3: Multitask S2T MSE ($\times 10^{-2}$) on TG80 across five UMAP cluster assignments.

		Cluster 1	**Cluster 2**	**Cluster 3**	**Cluster 4**	**Cluster 5**
ID	EGNO	44.23±0.68	95.52±0.73	141.16±0.21	150.92±0.11	107.47±0.36
	ATOM	**9.71**±0.75	**18.26**±1.58	**16.82**±1.46	**16.93**±3.65	**17.20**±0.46
	Gap	78.04%	80.89%	88.09%	88.78%	83.99%
OOD	MACE	134.26	224.12	325.97	316.26	229.64
	EGNO	45.95±0.80	115.43±13.23	151.74±0.57	163.90±0.69	113.68±2.50
	EGNN-S	45.44±0.57	7386.15±6931.89	152.72±0.83	464.22±509.48	114.30±0.79
	EGNN-R	44.88±0.68	109.62±1.92	148.05±0.70	161.54±0.68	110.10±0.96
	ATOM	**35.05**±0.97	**106.99**±104.64	**60.95**±4.86	**66.68**±0.96	**47.49**±1.59
	Gap	21.93%	2.40%	58.83%	58.71%	56.88%

4.2 MULTITASK LEARNING ON TG80

We pretrain ATOM on TG80, scaling to six attention blocks with a hidden size of 256. We select stochastic horizons $\Delta T \sim \mathrm{LogUnif}(8\,\mathrm{fs}, 24\,000\,\mathrm{fs})$ and use a five-fold, cluster-based cross-validation. Specifically, we compute ECFP-4 fingerprints (Rogers & Hahn, 2010), embed them using UMAP (McInnes et al., 2018), and apply agglomerative clustering (Ward, 1963) to partition compounds into ten disjoint clusters. The folds are then formed by holding out clusters, ensuring that the train/validation/test sets occupy distinct regions of chemical space. This cluster-wise protocol minimizes leakage and more closely reflects the prospective scientific setting in which models must generalize to unseen molecules. Cluster-based approaches present more challenging generalization problems than random splits or common chemical-scaffold-based splits (Guo et al., 2024). In Appendix E.2, we also consider pretraining on a standard random split of molecules.

Table 3 benchmarks ATOM by assessing both *in-distribution* (ID) and *out-of-domain* (OOD) S2T performance. For the *in-distribution* setting, we train, validate, and test on molecules from the same cluster. We observe that ATOM outperforms existing baselines by an average of 83.96% in terms of S2T MSE. We then assess *out-of-domain* (OOD) generalization performance by predicting the dynamics of unseen compounds drawn from disjoint clusters. Under OOD settings, ATOM nearly halves the S2T MSE of EGNO, with an average improvement of 39.74% across five cluster splits. Notably, OOD ATOM beats ID EGNO performance in four of five folds. This striking zero-shot generalization, realized without any exposure to the test molecules, confirms that ATOM uniquely learns robust, transferable knowledge of molecular dynamics. In Appendix E.2, we show similar outperformance in S2S prediction. In Appendix F.2, we show that the significantly improved multitask performance comes with a modest overhead in training time and in inference latency.

4.3 TEMPORAL GAP AND TIMESTEP INVARIANCE PROPERTIES

ΔT Invariance. We evaluate the performance of pretrained ATOM (at fixed $\Delta T = 3000$) with varying ΔT at inference. We compare ATOM, EGNO, and EGNN on S2T MSE by fixing $P = 8$ and sweeping ΔT logarithmically from 10 to 10 000 fs on an in-distribution (Cluster 1) multitask model. In Figure 3, we show that ATOM maintains its extrapolation advantage across the range compared to

EGNO, particularly at larger ΔT. Ablating T-RoPE (NoPE) removes this advantage by exhibiting an EGNO-like error trend with substantially higher MSE. This underscores T-RoPE's role in stable time-gap extrapolation.

P **Invariance.** Following the discretization invariance in neural operators, we expect ATOM and EGNO models to show consistent MSE as P varies under uniform discretization (Kovachki et al., 2021). Figure 4 confirms such a conjecture by showing that multitask ATOM pretrained at $P = 8$ maintain constant S2T MSE as P ranges from 4 to 24 at inference.

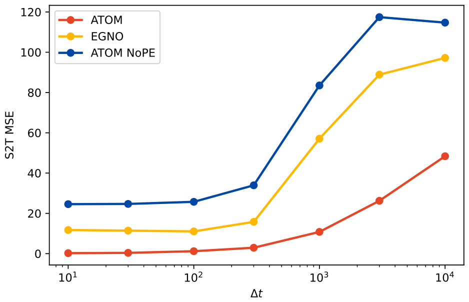

Figure 3: Pretrained ($\Delta T = 3000$, ID) multitask S2T MSE across varying ΔT values.

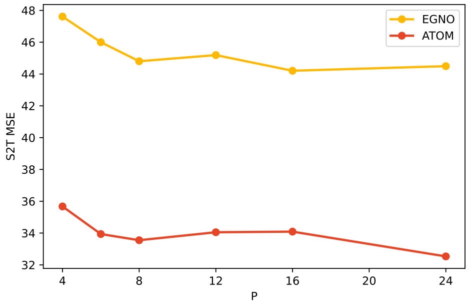

Figure 4: Pretrained ($P = 8$) ATOM and EGNO are discretization invariant, showing stable S2T MSE.

4.4 ABLATION STUDIES

We perform extensive ablations to assess each design choice in ATOM. For single-task performance (Fig. 5) and multitask performance (Fig. 6), we independently toggle components and measure their contributions. Our analysis focuses on equivariant lifting, T-RoPE, label-noise regularization, heterogeneous attention, and random-walk positional encoding (under multitask pretraining).

Table 4: S2T MSE ($\times 10^{-2}$) of a fixed input frame rotated and unrotated by an $\mathrm{SO}(3)$ matrix.

	ATOM	No equivariant Lift
Unrotated	$6.76_{\pm 0.69}$	$33.44_{\pm 23.42}$
Rotated	$73.04_{\pm 27.01}$	$660.97_{\pm 945.86}$
Gap	$66.28_{\pm 26.32}$	$627.53_{\pm 926.53}$

Equivariant lifting. We assess the quasi-equivariant design against a non-equivariant ATOM. As shown in Figure 5, replacing the equivariant lifting introduced in Section 3.2.1 with standard linear layers (no equivariant lifting) markedly degrades the performance of ATOM, increasing S2T MSE by 22.48. Consistently, Table 4 shows that non-equivariant lifting is vulnerable under $\mathrm{SO}(3)$ rotations of the trajectories, whereas the quasi-equivariant ATOM remains comparatively robust. Notably, the fully-equivariant variant of ATOM, described in appendix Appendix D.1, also underperforms ATOM in both single-task (Figure 5) and multitask (Figure 6) settings, with the gap exaggerated in the multitask setting. This aligns with recent findings on relaxed equivariance, suggesting that strict equivariance can limit model capacity and complicate the optimization process (Elhag et al., 2025). We present estimates of the quasi-equivariance ε in Appendix E.3.

Heterogeneous attention. We find that substituting heterogeneous temporal attention with standard self-attention on the phase space features increases S2S MSE by 0.47, suggesting that cross-attention enables access to non-trivial feature interactions.

Temporal Rotary Position Embedding (T-RoPE). In the single-task regime with fixed ΔT (Figure 5), T-RoPE contributes little to the performance of ATOM, as it effectively reduces to a constant rotational shift. By contrast, with stochastic ΔT, disabling T-RoPE (NoPE) increases MSE by 1.07, consistent with ATOM leveraging the τ parameter to encode variable time gaps (Figure 6). An EGNO-style sinusoidal positional encoding produces a similar performance degradation.

Label noise regularization. We also test the utility of label noise regularization as in Section 3.2.3. From Figure 5, we observe that removing augmented noise from the position and velocity features in-

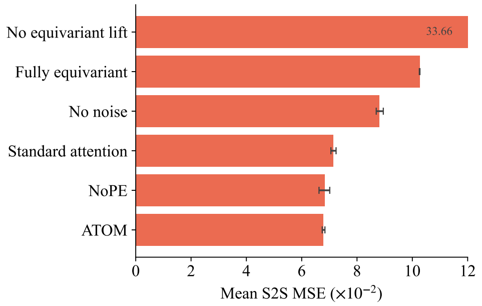

Figure 5: ATOM ablation on MD17 Aspirin.

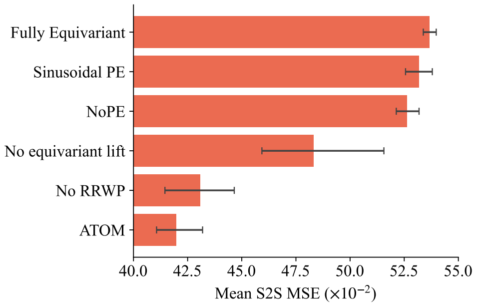

Figure 6: ATOM ablation on TG80 Cluster 1.

creased S2T MSE by 1.21. For the multitask ablation on TG80, we suppress label noise regularization, as the dataset is designed to be numerically stable with small noise.

RWPE. We assess random-walk positional encoding (RWPE) in the multitask pretraining. Figure 6 indicates that RWPE facilitates molecule identification, yielding improved multitask performance.

5 CONCLUSIONS

In this work, we demonstrate that carefully designed transformer neural operators enable zero-shot generalization to unseen chemical dynamics. Our experiments on MD17 demonstrate continued good single-task performance, and we present the first molecular neural operator that can successfully learn large molecule dynamics using MD22. Our multitask experiments show that our method learns transferable dynamics knowledge, even without explicit graph representations. In combination with our TG80 dataset, we provide a large-scale open-source benchmark and baselines to evaluate future models and spur further operator research with concrete scientific applicability.

Limitations We remark that TG80 does not contain trajectories for large molecules with more than 15 heavy atoms, despite their obvious chemical and pharmacological relevance. In follow-up work, we intend to enrich TG80 with such molecules, calculated with a higher-resolution DFT basis set, ωB97X-3c (Müller et al., 2023). Regarding ATOM, it lacks an explicit energy-based inductive bias, which may permit long-horizon drift. A natural extension is therefore a framewise energy head $E_\theta(\mathbf{x}_{t_p})$ with force supervision $\mathbf{F}_{t_p} = -\nabla_{\mathbf{x}_{t_p}} E_\theta(\mathbf{x}_{t_p})$. This energy term also defines the drift in the Langevin dynamics, where an additional stochastic term accounts for thermal perturbations of atomic positions. Incorporating such physics-informed stochastic dynamics into our operator learning framework is a natural next step, and we view this as a promising direction for future MD research.

REPRODUCIBILITY STATEMENT

We provide experiment details, such as choice of hyperparameters and other training configurations in Appendix F. In addition, we will release the TG80 dataset upon acceptance under MIT license for reproducibility.

REFERENCES

Uri Alon and Eran Yahav. On the Bottleneck of Graph Neural Networks and its Practical Implications, March 2021. URL `http://arxiv.org/abs/2006.05205`. arXiv:2006.05205 [cs].

Ilyes Batatia, Simon Batzner, Dávid Péter Kovács, Albert Musaelian, Gregor N. C. Simm, Ralf Drautz, Christoph Ortner, Boris Kozinsky, and Gábor Csányi. The Design Space of E(3)-Equivariant Atom-Centered Interatomic Potentials, 2022. URL `https://arxiv.org/abs/2205.06643`. _eprint: 2205.06643.

Ilyes Batatia, Dávid Péter Kovács, Gregor N. C. Simm, Christoph Ortner, and Gábor Csányi. MACE: Higher Order Equivariant Message Passing Neural Networks for Fast and Accurate Force Fields, January 2023. URL http://arxiv.org/abs/2206.07697. arXiv:2206.07697 [stat].

Simon Batzner, Albert Musaelian, Lixin Sun, Mario Geiger, Jonathan P. Mailoa, Mordechai Kornbluth, Nicola Molinari, Tess E. Smidt, and Boris Kozinsky. E(3)-equivariant graph neural networks for data-efficient and accurate interatomic potentials. *Nature Communications*, 13(1), May 2022. ISSN 2041-1723. doi: 10.1038/s41467-022-29939-5. URL http://dx.doi.org/10.1038/s41467-022-29939-5. Publisher: Springer Science and Business Media LLC.

Maya Bechler-Speicher, Ben Finkelshtein, Fabrizio Frasca, Luis Müller, Jan Tönshoff, Antoine Siraudin, Viktor Zaverkin, Michael M. Bronstein, Mathias Niepert, Bryan Perozzi, Mikhail Galkin, and Christopher Morris. Position: Graph Learning Will Lose Relevance Due To Poor Benchmarks, 2025. URL https://arxiv.org/abs/2502.14546. _eprint: 2502.14546.

Samy Bengio, Oriol Vinyals, Navdeep Jaitly, and Noam Shazeer. Scheduled Sampling for Sequence Prediction with Recurrent Neural Networks, 2015. URL https://arxiv.org/abs/1506.03099. _eprint: 1506.03099.

Shane Bergsma, Timothy Zeyl, and Lei Guo. SutraNets: Sub-series Autoregressive Networks for Long-Sequence, Probabilistic Forecasting, 2023. URL https://arxiv.org/abs/2312.14880. _eprint: 2312.14880.

Filippo Bigi, Sanggyu Chong, Agustinus Kristiadi, and Michele Ceriotti. FlashMD: long-stride, universal prediction of molecular dynamics, October 2025. URL http://arxiv.org/abs/2505.19350. arXiv:2505.19350 [physics].

Vaibhav Bihani, Utkarsh Pratiush, Sajid Mannan, Tao Du, Zhimin Chen, Santiago Miret, Matthieu Micoulaut, Morten M. Smedskjaer, Sayan Ranu, and N. M. Anoop Krishnan. EGraFFBench: Evaluation of Equivariant Graph Neural Network Force Fields for Atomistic Simulations, 2023. URL https://arxiv.org/abs/2310.02428. _eprint: 2310.02428.

Evan E. Bolton, Jie Chen, Sunghwan Kim, Lianyi Han, Siqian He, Wenyao Shi, Vahan Simonyan, Yan Sun, Paul A. Thiessen, Jiyao Wang, Bo Yu, Jian Zhang, and Stephen H. Bryant. PubChem3D: a new resource for scientists. *Journal of cheminformatics*, 3(1):32, September 2011. ISSN 1758-2946. doi: 10.1186/1758-2946-3-32. Place: England.

Johann Brehmer, Pim de Haan, Sönke Behrends, and Taco Cohen. Geometric Algebra Transformer, 2023. URL https://arxiv.org/abs/2305.18415. _eprint: 2305.18415.

Shaked Brody, Uri Alon, and Eran Yahav. How Attentive are Graph Attention Networks?, 2022. URL https://arxiv.org/abs/2105.14491. _eprint: 2105.14491.

Michael M. Bronstein, Joan Bruna, Taco Cohen, and Petar Veličković. Geometric Deep Learning: Grids, Groups, Graphs, Geodesics, and Gauges, 2021. URL https://arxiv.org/abs/2104.13478. _eprint: 2104.13478.

Andrey Bryutkin, Jiahao Huang, Zhongying Deng, Guang Yang, Carola-Bibiane Schönlieb, and Angelica Aviles-Rivero. HAMLET: Graph Transformer Neural Operator for Partial Differential Equations, 2024. URL https://arxiv.org/abs/2402.03541. _eprint: 2402.03541.

Eike Caldeweyher, Sebastian Ehlert, Andreas Hansen, Hagen Neugebauer, Sebastian Spicher, Christoph Bannwarth, and Stefan Grimme. A generally applicable atomic-charge dependent London dispersion correction. *The Journal of Chemical Physics*, 150(15), April 2019. ISSN 1089-7690. doi: 10.1063/1.5090222. URL http://dx.doi.org/10.1063/1.5090222. Publisher: AIP Publishing.

Eike Caldeweyher, Jan-Michael Mewes, Sebastian Ehlert, and Stefan Grimme. Extension and evaluation of the D4 London-dispersion model for periodic systems. *Physical Chemistry Chemical Physics*, 22(16):8499–8512, 2020. ISSN 1463-9084. doi: 10.1039/d0cp00502a. URL http://dx.doi.org/10.1039/D0CP00502A. Publisher: Royal Society of Chemistry (RSC).

David A. Case, Hasan Metin Aktulga, Kellon Belfon, David S. Cerutti, G. Andrés Cisneros, Vinícius Wilian D. Cruzeiro, Negin Forouzesh, Timothy J. Giese, Andreas W. Götz, Holger Gohlke, Saeed Izadi, Koushik Kasavajhala, Mehmet C. Kaymak, Edward King, Tom Kurtzman, Tai-Sung Lee, Pengfei Li, Jian Liu, Tyler Luchko, Ray Luo, Madushanka Manathunga, Matias R. Machado, Hai Minh Nguyen, Kurt A. O'Hearn, Alexey V. Onufriev, Feng Pan, Sergio Pantano, Ruxi Qi, Ali Rahnamoun, Ali Risheh, Stephan Schott-Verdugo, Akhil Shajan, Jason Swails, Junmei Wang, Haixin Wei, Xiongwu Wu, Yongxian Wu, Shi Zhang, Shiji Zhao, Qiang Zhu, Thomas E. III Cheatham, Daniel R. Roe, Adrian Roitberg, Carlos Simmerling, Darrin M. York, Maria C. Nagan, and Kenneth M. Jr. Merz. AmberTools. *Journal of Chemical Information and Modeling*, 63(20):6183–6191, October 2023. ISSN 1549-9596. doi: 10.1021/acs.jcim.3c01153. URL https://doi.org/10.1021/acs.jcim.3c01153. Publisher: American Chemical Society.

Stefan Chmiela, Alexandre Tkatchenko, Huziel E. Sauceda, Igor Poltavsky, Kristof T. Schütt, and Klaus-Robert Müller. Machine learning of accurate energy-conserving molecular force fields. *Science Advances*, 3(5):e1603015, 2017. doi: 10.1126/sciadv.1603015. URL https://www.science.org/doi/abs/10.1126/sciadv.1603015. _eprint: https://www.science.org/doi/pdf/10.1126/sciadv.1603015.

Stefan Chmiela, Valentin Vassilev-Galindo, Oliver T. Unke, Adil Kabylda, Huziel E. Sauceda, Alexandre Tkatchenko, and Klaus-Robert Müller. Accurate global machine learning force fields for molecules with hundreds of atoms. *Science Advances*, 9(2), January 2023. ISSN 2375-2548. doi: 10.1126/sciadv.adf0873. URL http://dx.doi.org/10.1126/sciadv.adf0873. Publisher: American Association for the Advancement of Science (AAAS).

Anders S Christensen and O Anatole von Lilienfeld. On the role of gradients for machine learning of molecular energies and forces. *Mach. Learn. Sci. Technol.*, 1(4):045018, October 2020. Publisher: IOP Publishing.

Alex Damian, Tengyu Ma, and Jason D. Lee. Label Noise SGD Provably Prefers Flat Global Minimizers, December 2021. URL http://arxiv.org/abs/2106.06530. arXiv:2106.06530 [cs].

J Dauparas, I Anishchenko, N Bennett, H Bai, R J Ragotte, L F Milles, B I M Wicky, A Courbet, R J de Haas, N Bethel, P J Y Leung, T F Huddy, S Pellock, D Tischer, F Chan, B Koepnick, H Nguyen, A Kang, B Sankaran, A K Bera, N P King, and D Baker. Robust deep learning-based protein sequence design using ProteinMPNN. *Science (American Association for the Advancement of Science)*, 378(6615):49–56, 2022. ISSN 0036-8075. Backup Publisher: Lawrence Berkeley National Laboratory (LBNL), Berkeley, CA (United States) Place: United States Publisher: The American Association for the Advancement of Science.

Marco De Vivo, Matteo Masetti, Giovanni Bottegoni, and Andrea Cavalli. Role of Molecular Dynamics and Related Methods in Drug Discovery. *Journal of Medicinal Chemistry*, 59(9): 4035–4061, May 2016. ISSN 0022-2623. doi: 10.1021/acs.jmedchem.5b01684. URL https://doi.org/10.1021/acs.jmedchem.5b01684. Publisher: American Chemical Society.

Blaise Delattre, Quentin Barthélemy, Alexandre Araujo, and Alexandre Allauzen. Efficient Bound of Lipschitz Constant for Convolutional Layers by Gram Iteration, June 2023. URL http://arxiv.org/abs/2305.16173. arXiv:2305.16173 [cs].

Ron O. Dror, Robert M. Dirks, J. P. Grossman, Huafeng Xu, and David E. Shaw. Biomolecular simulation: a computational microscope for molecular biology. *Annual Review of Biophysics*, 41: 429–452, 2012. ISSN 1936-1238. doi: 10.1146/annurev-biophys-042910-155245.

Alexandre Duval, Simon V. Mathis, Chaitanya K. Joshi, Victor Schmidt, Santiago Miret, Fragkiskos D. Malliaros, Taco Cohen, Pietro Lio, Yoshua Bengio, and Michael Bronstein. A Hitchhiker's Guide to Geometric GNNs for 3D Atomic Systems. pp. arXiv:2312.07511, December 2023. doi: 10.48550/arXiv.2312.07511.

Vijay Prakash Dwivedi, Anh Tuan Luu, Thomas Laurent, Yoshua Bengio, and Xavier Bresson. Graph Neural Networks with Learnable Structural and Positional Representations, 2022. URL https://arxiv.org/abs/2110.07875. _eprint: 2110.07875.

Peter Eastman, Pavan Kumar Behara, David L. Dotson, Raimondas Galvelis, John E. Herr, Josh T. Horton, Yuezhi Mao, John D. Chodera, Benjamin P. Pritchard, Yuanqing Wang, Gianni De Fabritiis, and Thomas E. Markland. SPICE, A Dataset of Drug-like Molecules and Peptides for Training Machine Learning Potentials. *Scientific Data*, 10(1), January 2023. ISSN 2052-4463. doi: 10.1038/s41597-022-01882-6. URL http://dx.doi.org/10.1038/s41597-022-01882-6. Publisher: Springer Science and Business Media LLC.

Ahmed A. Elhag, T. Konstantin Rusch, Francesco Di Giovanni, and Michael Bronstein. Relaxed Equivariance via Multitask Learning, 2025. URL https://arxiv.org/abs/2410.17878. _eprint: 2410.17878.

Fabian B. Fuchs, Daniel E. Worrall, Volker Fischer, and Max Welling. SE(3)-Transformers: 3D Roto-Translation Equivariant Attention Networks. *arXiv e-prints*, pp. arXiv:2006.10503, June 2020. doi: 10.48550/arXiv.2006.10503. _eprint: 2006.10503.

Nicholas Gao, Eike Eberhard, and Stephan Günnemann. Learning Equivariant Non-Local Electron Density Functionals, October 2024. URL http://arxiv.org/abs/2410.07972. arXiv:2410.07972 [cs] version: 1.

Victor Garcia Satorras, Emiel Hoogeboom, and Max Welling. E(n) Equivariant Graph Neural Networks. *arXiv e-prints*, pp. arXiv:2102.09844, February 2021. doi: 10.48550/arXiv.2102.09844. _eprint: 2102.09844.

Johannes Gasteiger, Florian Becker, and Stephan Günnemann. GemNet: Universal Directional Graph Neural Networks for Molecules. pp. arXiv:2106.08903, June 2021. doi: 10.48550/arXiv.2106.08903.

Mario Geiger and Tess Smidt. e3nn: Euclidean Neural Networks, 2022. URL https://arxiv.org/abs/2207.09453. _eprint: 2207.09453.

Qianrong Guo, Saiveth Hernandez-Hernandez, and Pedro J. Ballester. Scaffold Splits Overestimate Virtual Screening Performance, June 2024. URL http://arxiv.org/abs/2406.00873. arXiv:2406.00873 [q-bio].

Zhongkai Hao, Zhengyi Wang, Hang Su, Chengyang Ying, Yinpeng Dong, Songming Liu, Ze Cheng, Jian Song, and Jun Zhu. GNOT: A General Neural Operator Transformer for Operator Learning, June 2023. URL http://arxiv.org/abs/2302.14376. arXiv:2302.14376.

Zhongkai Hao, Chang Su, Songming Liu, Julius Berner, Chengyang Ying, Hang Su, Anima Anandkumar, Jian Song, and Jun Zhu. DPOT: Auto-Regressive Denoising Operator Transformer for Large-Scale PDE Pre-Training, May 2024. URL http://arxiv.org/abs/2403.03542. arXiv:2403.03542 [cs].

Jeff Z. HaoChen, Colin Wei, Jason D. Lee, and Tengyu Ma. Shape Matters: Understanding the Implicit Bias of the Noise Covariance, June 2020. URL http://arxiv.org/abs/2006.08680. arXiv:2006.08680 [cs].

G Harper, S Pickett, and D. Green. (Research Papers) Design of a Compound Screening Collection for use in High Throughput Screening. *Combinatorial Chemistry & High Throughput Screening*, 7 (1):63–70, February 2004. ISSN 1386-2073. doi: 10.2174/138620704772884832. URL http://dx.doi.org/10.2174/138620704772884832. Publisher: Bentham Science Publishers Ltd.

Charles R. Harris, K. Jarrod Millman, Stéfan J. van der Walt, Ralf Gommers, Pauli Virtanen, David Cournapeau, Eric Wieser, Julian Taylor, Sebastian Berg, Nathaniel J. Smith, Robert Kern, Matti Picus, Stephan Hoyer, Marten H. van Kerkwijk, Matthew Brett, Allan Haldane, Jaime Fernández del Río, Mark Wiebe, Pearu Peterson, Pierre Gérard-Marchant, Kevin Sheppard, Tyler Reddy, Warren Weckesser, Hameer Abbasi, Christoph Gohlke, and Travis E. Oliphant. Array programming with NumPy. *Nature*, 585(7825):357–362, September 2020. doi: 10.1038/s41586-020-2649-2. URL https://doi.org/10.1038/s41586-020-2649-2. Publisher: Springer Science and Business Media LLC.

Jacob Helwig, Xuan Zhang, Cong Fu, Jerry Kurtin, Stephan Wojtowytsch, and Shuiwang Ji. Group Equivariant Fourier Neural Operators for Partial Differential Equations, 2023. URL https://arxiv.org/abs/2306.05697. _eprint: 2306.05697.

Tim Hsu, Babak Sadigh, Vasily Bulatov, and Fei Zhou. Score Dynamics: Scaling Molecular Dynamics with Picoseconds Time Steps via Conditional Diffusion Model. *Journal of Chemical Theory and Computation*, 20(6):2335–2348, March 2024. ISSN 1549-9618, 1549-9626. doi: 10.1021/acs.jctc.3c01361. URL https://pubs.acs.org/doi/10.1021/acs.jctc.3c01361.

Wenbing Huang, Jiaqi Han, Yu Rong, Tingyang Xu, Fuchun Sun, and Junzhou Huang. Equivariant Graph Mechanics Networks with Constraints, 2022. URL https://arxiv.org/abs/2203.06442. _eprint: 2203.06442.

Keller Jordan. NanoGPT Speedrun 11/06/24, June 2024. URL https://github.com/KellerJordan/modded-nanogpt/blob/master/records/011625_Sub3Min/1d3bd93b-a69e-4118-aeb8-8184239d7566.txt.

Keller Jordan, Yuchen Jin, Vlado Boza, Jiacheng You, Franz Cesista, Laker Newhouse, and Jeremy Bernstein. Muon: An optimizer for hidden layers in neural networks, 2024. URL https://kellerjordan.github.io/posts/muon/.

Keller Jordan, Jiacheng You, Cesista Franz Louis, and Brendon Hogan. NanoGPT Speedrun 01/16/25, January 2025. URL https://github.com/KellerJordan/modded-nanogpt/blob/master/records/011625_Sub3Min/1d3bd93b-a69e-4118-aeb8-8184239d7566.txt.

Sékou-Oumar Kaba, Arnab Kumar Mondal, Yan Zhang, Yoshua Bengio, and Siamak Ravanbakhsh. Equivariance with Learned Canonicalization Functions, July 2023. URL http://arxiv.org/abs/2211.06489. arXiv:2211.06489 [cs].

Hyeongchan Kim. pytorch_optimizer: optimizer & lr scheduler & loss function collections in PyTorch, September 2021. URL https://github.com/kozistr/pytorch_optimizer.

Leon Klein, Andrew Y. K. Foong, Tor Erlend Fjelde, Bruno Mlodozeniec, Marc Brockschmidt, Sebastian Nowozin, Frank Noé, and Ryota Tomioka. Timewarp: Transferable Acceleration of Molecular Dynamics by Learning Time-Coarsened Dynamics, December 2023. URL http://arxiv.org/abs/2302.01170. arXiv:2302.01170 [stat].

Sebastian Kmiecik, Dominik Gront, Michal Kolinski, Lukasz Wieteska, Aleksandra Elzbieta Dawid, and Andrzej Kolinski. Coarse-Grained Protein Models and Their Applications. *Chemical Reviews*, 116(14):7898–7936, July 2016. ISSN 1520-6890. doi: 10.1021/acs.chemrev.6b00163.

Carter Knutson, Gihan Panapitiya, Rohith Varikoti, and Neeraj Kumar. Dynamic Molecular Graph-based Implementation for Biophysical Properties Prediction, 2022. URL https://arxiv.org/abs/2212.09991. _eprint: 2212.09991.

Arthur Kosmala, Johannes Gasteiger, Nicholas Gao, and Stephan Günnemann. Ewald-based Long-Range Message Passing for Molecular Graphs, June 2023. URL http://arxiv.org/abs/2303.04791. arXiv:2303.04791 [cs].

Nikola Kovachki, Zongyi Li, Burigede Liu, Kamyar Azizzadenesheli, Kaushik Bhattacharya, Andrew Stuart, and Anima Anandkumar. Neural Operator: Learning Maps Between Function Spaces. *arXiv e-prints*, pp. arXiv:2108.08481, August 2021. doi: 10.48550/arXiv.2108.08481. _eprint: 2108.08481.

Dávid Péter Kovács, J. Harry Moore, Nicholas J. Browning, Ilyes Batatia, Joshua T. Horton, Yixuan Pu, Venkat Kapil, William C. Witt, Ioan-Bogdan Magdău, Daniel J. Cole, and Gábor Csányi. MACE-OFF: Short-Range Transferable Machine Learning Force Fields for Organic Molecules. *Journal of the American Chemical Society*, 147(21):17598–17611, May 2025. ISSN 0002-7863. doi: 10.1021/jacs.4c07099. URL https://doi.org/10.1021/jacs.4c07099. Publisher: American Chemical Society.

G. Kresse and J. Furthmüller. Efficiency of ab-initio total energy calculations for metals and semiconductors using a plane-wave basis set. *Computational Materials Science*, 6(1):15–50, 1996. ISSN 0927-0256. doi: https://doi.org/10.1016/0927-0256(96)00008-0. URL https://www.sciencedirect.com/science/article/pii/0927025696000080.

Jonas Köhler, Leon Klein, and Frank Noé. Equivariant Flows: sampling configurations for multi-body systems with symmetric energies. *arXiv e-prints*, pp. arXiv:1910.00753, October 2019. doi: 10.48550/arXiv.1910.00753. _eprint: 1910.00753.

Greg Landrum, Paolo Tosco, Brian Kelley, Ricardo Rodriguez, David Cosgrove, Riccardo Vianello, sriniker, Peter Gedeck, Gareth Jones, Eisuke Kawashima, NadineSchneider, Dan Nealschneider, Andrew Dalke, Matt Swain, Brian Cole, Samo Turk, Aleksandr Savelev, tadhurst cdd, Alain Vaucher, Maciej Wójcikowski, Ichiru Take, Rachel Walker, Vincent F. Scalfani, Hussein Faara, Kazuya Ujihara, Daniel Probst, Juuso Lehtivarjo, guillaume godin, Axel Pahl, and Niels Maeder. rdkit/rdkit: 2025_03_2 (Q1 2025) Release, 2025. URL https://zenodo.org/doi/10.5281/zenodo.591637.

Ask Hjorth Larsen, Jens Jørgen Mortensen, Jakob Blomqvist, Ivano E. Castelli, Rune Christensen, Marcin Dułak, Jesper Friis, Michael N. Groves, Bjørk Hammer, Cory Hargus, Eric D. Hermes, Paul C. Jennings, Peter Bjerre Jensen, James Kermode, John R. Kitchin, Esben Leonhard Kolsbjerg, Joseph Kubal, Kristen Kaasbjerg, Steen Lysgaard, Jón Bergmann Maronsson, Tristan Maxson, Thomas Olsen, Lars Pastewka, Andrew Peterson, Carsten Rostgaard, Jakob Schiøtz, Ole Schütt, Mikkel Strange, Kristian S. Thygesen, Tejs Vegge, Lasse Vilhelmsen, Michael Walter, Zhenhua Zeng, and Karsten W. Jacobsen. The atomic simulation environment—a Python library for working with atoms. *Journal of Physics: Condensed Matter*, 29(27):273002, 2017. URL http://stacks.iop.org/0953-8984/29/i=27/a=273002.

Vu-Anh Le and Mehmet Dik. A Mathematical Analysis of Neural Operator Behaviors, October 2024. URL http://arxiv.org/abs/2410.21481. arXiv:2410.21481 [math].

Jianxiong Li, Boyang Li, Zhuoqiang Guo, Mingzhen Li, Enji Li, Lijun Liu, Guojun Yuan, Zhan Wang, Guangming Tan, and Weile Jia. Scaling Molecular Dynamics with ab initio Accuracy to 149 Nanoseconds per Day. In *SC24: International Conference for High Performance Computing, Networking, Storage and Analysis*, pp. 1–15. IEEE, November 2024. doi: 10.1109/sc41406.2024.00036. URL http://dx.doi.org/10.1109/SC41406.2024.00036.

Zijie Li, Kazem Meidani, and Amir Barati Farimani. Transformer for Partial Differential Equations' Operator Learning, 2023a. URL https://arxiv.org/abs/2205.13671. _eprint: 2205.13671.

Zongyi Li, Nikola Kovachki, Kamyar Azizzadenesheli, Burigede Liu, Kaushik Bhattacharya, Andrew Stuart, and Anima Anandkumar. Fourier Neural Operator for Parametric Partial Differential Equations, May 2021. URL http://arxiv.org/abs/2010.08895. arXiv:2010.08895.

Zongyi Li, Hongkai Zheng, Nikola Kovachki, David Jin, Haoxuan Chen, Burigede Liu, Kamyar Azizzadenesheli, and Anima Anandkumar. Physics-Informed Neural Operator for Learning Partial Differential Equations, 2023b. URL https://arxiv.org/abs/2111.03794. _eprint: 2111.03794.

Yi-Lun Liao and Tess Smidt. Equiformer: Equivariant Graph Attention Transformer for 3D Atomistic Graphs, 2023. URL https://arxiv.org/abs/2206.11990. _eprint: 2206.11990.

Alvaro Lobato, Miguel A. Salvadó, J. Manuel Recio, Mercedes Taravillo, and Valentín G. Baonza. Highs and Lows of Bond Lengths: Is There Any Limit? *Angewandte Chemie International Edition*, 60(31):17028–17036, June 2021. ISSN 1521-3773. doi: 10.1002/anie.202102967. URL http://dx.doi.org/10.1002/anie.202102967. Publisher: Wiley.

Ilya Loshchilov and Frank Hutter. Decoupled Weight Decay Regularization. *arXiv e-prints*, pp. arXiv:1711.05101, November 2017. doi: 10.48550/arXiv.1711.05101. _eprint: 1711.05101.

Shitong Luo, Chence Shi, Minkai Xu, and Jian Tang. Predicting Molecular Conformation via Dynamic Graph Score Matching. In M. Ranzato, A. Beygelzimer, Y. Dauphin, P. S. Liang, and J. Wortman

Vaughan (eds.), *Advances in Neural Information Processing Systems*, volume 34, pp. 19784–19795. Curran Associates, Inc., 2021. URL https://proceedings.neurips.cc/paper_files/paper/2021/file/a45a1d12ee0fb7f1f872ab91da18f899-Paper.pdf.

Liheng Ma, Chen Lin, Derek Lim, Adriana Romero-Soriano, Puneet K. Dokania, Mark Coates, Philip Torr, and Ser-Nam Lim. Graph Inductive Biases in Transformers without Message Passing, May 2023. URL http://arxiv.org/abs/2305.17589. arXiv:2305.17589 [cs].

Hans Matter. Selecting Optimally Diverse Compounds from Structure Databases: A Validation Study of Two-Dimensional and Three-Dimensional Molecular Descriptors. *Journal of Medicinal Chemistry*, 40(8):1219–1229, April 1997. ISSN 1520-4804. doi: 10.1021/jm960352+. URL http://dx.doi.org/10.1021/jm960352. Publisher: American Chemical Society (ACS).

Leland McInnes, John Healy, and James Melville. UMAP: Uniform Manifold Approximation and Projection for Dimension Reduction. *arXiv e-prints*, pp. arXiv:1802.03426, February 2018. doi: 10.48550/arXiv.1802.03426. _eprint: 1802.03426.

Janosch Menke, Joana Massa, and Oliver Koch. Natural product scores and fingerprints extracted from artificial neural networks. *Computational and Structural Biotechnology Journal*, 19:4593–4602, 2021. ISSN 2001-0370. doi: 10.1016/j.csbj.2021.07.032. URL http://dx.doi.org/10.1016/j.csbj.2021.07.032. Publisher: Elsevier BV.

Albert Musaelian, Simon Batzner, Anders Johansson, Lixin Sun, Cameron J. Owen, Mordechai Kornbluth, and Boris Kozinsky. Learning Local Equivariant Representations for Large-Scale Atomistic Dynamics, 2022. URL https://arxiv.org/abs/2204.05249. _eprint: 2204.05249.

Marcel Müller, Andreas Hansen, and Stefan Grimme. omegaB97X-3c: A composite range-separated hybrid DFT method with a molecule-optimized polarized valence double-zeta basis set. *The Journal of Chemical Physics*, 158(1), January 2023. ISSN 1089-7690. doi: 10.1063/5.0133026. URL http://dx.doi.org/10.1063/5.0133026. Publisher: AIP Publishing.

Frank Neese. Software update: The ORCA program system—Version 5.0. *WIREs Computational Molecular Science*, 12(5):e1606, 2022. doi: https://doi.org/10.1002/wcms.1606. URL https://wires.onlinelibrary.wiley.com/doi/abs/10.1002/wcms.1606. _eprint: https://wires.onlinelibrary.wiley.com/doi/pdf/10.1002/wcms.1606.

Eldho Nv, Feller Se, Tristram-Nagle S, Polozov Iv, and Gawrisch K. Polyunsaturated docosahexaenoic vs docosapentaenoic acid-differences in lipid matrix properties from the loss of one double bond. *Journal of the American Chemical Society*, 125(21), May 2003. ISSN 0002-7863. doi: 10.1021/ja029029o. URL https://pubmed.ncbi.nlm.nih.gov/12785780/. Publisher: J Am Chem Soc.

Adam Paszke, Sam Gross, Francisco Massa, Adam Lerer, James Bradbury, Gregory Chanan, Trevor Killeen, Zeming Lin, Natalia Gimelshein, Luca Antiga, Alban Desmaison, Andreas Köpf, Edward Yang, Zach DeVito, Martin Raison, Alykhan Tejani, Sasank Chilamkurthy, Benoit Steiner, Lu Fang, Junjie Bai, and Soumith Chintala. PyTorch: An Imperative Style, High-Performance Deep Learning Library. *arXiv e-prints*, pp. arXiv:1912.01703, December 2019. doi: 10.48550/arXiv.1912.01703. URL https://ui.adsabs.harvard.edu/abs/2019arXiv191201703P.

John P. Perdew, Kieron Burke, and Matthias Ernzerhof. Generalized Gradient Approximation Made Simple. *Physical Review Letters*, 77(18):3865–3868, October 1996. ISSN 1079-7114. doi: 10.1103/physrevlett.77.3865. URL http://dx.doi.org/10.1103/PhysRevLett.77.3865. Publisher: American Physical Society (APS).

David Rogers and Mathew Hahn. Extended-Connectivity Fingerprints. *Journal of chemical information and modeling*, 50(5):742–754, May 2010. ISSN 1549-9596. doi: 10.1021/ci100050t.

David J. Rogers and Taffee T. Tanimoto. A Computer Program for Classifying Plants. *Science*, 132:1115–1118, October 1960. ISSN 0036-8075. doi: 10.1126/science.132.3434.1115.

Mathias Schreiner, Ole Winther, and Simon Olsson. Implicit Transfer Operator Learning: Multiple Time-Resolution Surrogates for Molecular Dynamics, October 2023. URL http://arxiv.org/abs/2305.18046. arXiv:2305.18046 [physics].

Peter Schwerdtfeger and David J. Wales. 100 Years of the Lennard-Jones Potential. *Journal of Chemical Theory and Computation*, 20(9):3379–3405, May 2024. ISSN 1549-9618. doi: 10.1021/acs.jctc.4c00135. URL https://doi.org/10.1021/acs.jctc.4c00135. Publisher: American Chemical Society.

Chence Shi, Shitong Luo, Minkai Xu, and Jian Tang. Learning Gradient Fields for Molecular Conformation Generation, 2021. URL https://arxiv.org/abs/2105.03902. _eprint: 2105.03902.

Frederick Stein, Jürg Hutter, and Vladimir V. Rybkin. Double-Hybrid DFT Functionals for the Condensed Phase: Gaussian and Plane Waves Implementation and Evaluation. *Molecules*, 25(21), 2020. ISSN 1420-3049. doi: 10.3390/molecules25215174. URL https://www.mdpi.com/1420-3049/25/21/5174.

Jianlin Su, Yu Lu, Shengfeng Pan, Ahmed Murtadha, Bo Wen, and Yunfeng Liu. RoFormer: Enhanced Transformer with Rotary Position Embedding, November 2023. URL http://arxiv.org/abs/2104.09864. arXiv:2104.09864 [cs].

Souhaib Ben Taieb and Amir F. Atiya. A Bias and Variance Analysis for Multistep-Ahead Time Series Forecasting. *IEEE Transactions on Neural Networks and Learning Systems*, 27(1):62–76, 2016. doi: 10.1109/TNNLS.2015.2411629.

Fabian L Thiemann, Thiago Reschützegger, Massimiliano Esposito, Tseden Taddese, Juan D Olarte-Plata, and Fausto Martelli. Force-free molecular dynamics through autoregressive equivariant networks. *arXiv preprint arXiv:2503.23794*, 2025.

Nathaniel Thomas, Tess Smidt, Steven Kearnes, Lusann Yang, Li Li, Kai Kohlhoff, and Patrick Riley. Tensor field networks: Rotation- and translation-equivariant neural networks for 3D point clouds. *arXiv e-prints*, pp. arXiv:1802.08219, February 2018. doi: 10.48550/arXiv.1802.08219. _eprint: 1802.08219.

Joe H. Ward. Hierarchical Grouping to Optimize an Objective Function. *Journal of the American Statistical Association*, 58(301):236–244, 1963. doi: 10.1080/01621459.1963.10500845. URL https://www.tandfonline.com/doi/abs/10.1080/01621459.1963.10500845. Publisher: Taylor & Francis _eprint: https://www.tandfonline.com/doi/pdf/10.1080/01621459.1963.10500845.

Florian Weigend and Reinhart Ahlrichs. Balanced basis sets of split valence, triple zeta valence and quadruple zeta valence quality for H to Rn: Design and assessment of accuracy. *Physical Chemistry Chemical Physics*, 7(18):3297, 2005. ISSN 1463-9084. doi: 10.1039/b508541a. URL http://dx.doi.org/10.1039/B508541A. Publisher: Royal Society of Chemistry (RSC).

Maurice Weiler, Mario Geiger, Max Welling, Wouter Boomsma, and Taco Cohen. 3D Steerable CNNs: Learning Rotationally Equivariant Features in Volumetric Data, 2018. URL https://arxiv.org/abs/1807.02547. _eprint: 1807.02547.

Lukas Wittmann, Igor Gordiy, Marvin Friede, Benjamin Helmich-Paris, Stefan Grimme, Andreas Hansen, and Markus Bursch. Extension of the D3 and D4 London dispersion corrections to the full actinides series. *Physical Chemistry Chemical Physics*, 26(32):21379–21394, 2024. ISSN 1463-9084. doi: 10.1039/d4cp01514b. URL http://dx.doi.org/10.1039/D4CP01514B. Publisher: Royal Society of Chemistry (RSC).

Wenxuan Wu, Zhongang Qi, and Li Fuxin. PointConv: Deep Convolutional Networks on 3D Point Clouds, 2020. URL https://arxiv.org/abs/1811.07246. _eprint: 1811.07246.

Minkai Xu, Lantao Yu, Yang Song, Chence Shi, Stefano Ermon, and Jian Tang. GeoDiff: a Geometric Diffusion Model for Molecular Conformation Generation, 2022. URL https://arxiv.org/abs/2203.02923. _eprint: 2203.02923.

Minkai Xu, Jiaqi Han, Aaron Lou, Jean Kossaifi, Arvind Ramanathan, Kamyar Azizzadenesheli, Jure Leskovec, Stefano Ermon, and Anima Anandkumar. Equivariant Graph Neural Operator for Modeling 3D Dynamics, June 2024. URL http://arxiv.org/abs/2401.11037. arXiv:2401.11037.

Ziyang Yu, Wenbing Huang, and Yang Liu. UniSim: A Unified Simulator for Time-Coarsened Dynamics of Biomolecules, October 2025. URL http://arxiv.org/abs/2506.03157. arXiv:2506.03157 [q-bio].

Ziqiao Zhang, Bangyi Zhao, Ailin Xie, Yatao Bian, and Shuigeng Zhou. Activity Cliff Prediction: Dataset and Benchmark, February 2023. URL http://arxiv.org/abs/2302.07541. arXiv:2302.07541 [q-bio].

Tianze Zheng, Weihao Gao, and Chong Wang. Learning Large-Time-Step Molecular Dynamics with Graph Neural Networks, December 2021. URL http://arxiv.org/abs/2111.15176. arXiv:2111.15176 [physics].

Anthony Zhou, Cooper Lorsung, AmirPouya Hemmasian, and Amir Barati Farimani. Strategies for Pretraining Neural Operators, October 2024a. URL http://arxiv.org/abs/2406.08473. arXiv:2406.08473 [cs].

Zhanchao Zhou, Tianyi Wu, Zhiyun Jiang, and Zhenzhong Lan. Value Residual Learning For Alleviating Attention Concentration In Transformers, 2024b. URL https://arxiv.org/abs/2410.17897. _eprint: 2410.17897.

APPENDICES

A LLM ACKNOWLEDGMENT

The authors acknowledge the use of LLM for grammar corrections and for improving the clarity of the manuscript. The LLM was not used for generating original ideas, content, or experimental results. All conceptual contributions, analyses, and conclusions presented in this work are entirely from the authors.

B BACKGROUND

This section provides an introduction to the preliminaries of group theory.

B.1 GROUPS

A group $(G, \circ)$ consists of a non-empty set G and a binary operation $\circ : G \times G \to G$ satisfying the following axioms:

1. **Closure:** For all $a, b \in G$, the result of the operation $a \circ b$ is also in G: $a \circ b \in G$.
2. **Identity Element:** There exists an element $e \in G$ such that, for all $a \in G$, $a \circ e = e \circ a = a$.
3. **Associativity:** For all $a, b, c \in G$, $(a \circ b) \circ c = a \circ (b \circ c)$.
4. **Inverses:** For each $a \in G$, there exists an element $a^{-1} \in G$ such that $a \circ a^{-1} = a^{-1} \circ a = e$.

In general, not all groups are abelian. That is, the binary operation $\circ$ does not necessarily commute: $g \circ h = h \circ g, \forall g, h \in G$.

B.2 GROUP REPRESENTATIONS

A group representation is a homomorphism $\rho : G \to GL(V)$ that assigns an $n \times n$ matrix to each group element $g \in G$, realizing it as a linear transformation. Representations must preserve the binary operation for all members of the group G such that:

$$\rho(g \circ h) = \rho(g)\rho(h), \quad \forall g, h \in G.$$

A representation $\rho(g)$ is reducible if it can be represented as the direct sum of other representations:

$$\rho(g) = \rho_1(g) \oplus \rho_2(g), \quad \forall g \in G.$$

For example, a reducible 4×4 representation of $SU(2)$ can be decomposed into two 2×2 sub-representations:

$$\rho(g) = \begin{bmatrix} \rho_1(g) & 0 \\ 0 & \rho_2(g) \end{bmatrix}, \quad \forall g \in SU(2),$$

where $\rho_1(g)$ and $\rho_2(g)$ are the following irreducible representations of $SU(2)$:

$$\rho_1(g) = \begin{bmatrix} e^{i\theta} & 0 \\ 0 & e^{-i\theta} \end{bmatrix}, \quad \rho_2(g) = \begin{bmatrix} e^{i\phi} & 0 \\ 0 & e^{-i\phi} \end{bmatrix}.$$

By contrast, irreducible representations or *irreps* cannot be represented as such a direct sum. Formally, they have no non-trivial invariant subspaces $W \subset V$ such that $\rho(g)W \subset W, \forall g \in G$.

Representing inputs as irreps ensures equivariance by constraining each feature to transform predictably under group actions. Given $V = \bigoplus_i V_i$ with irreps V_i, the transformation of an input $x \in V$ under $g \in G$ is:

$$\rho(g)x = \bigoplus_i \rho_i(g)x_i.$$

Each component x_i transforms independently according to ρ_i, preserving symmetry. Scalars remain invariant, while vectors rotate according to standard representations. This decomposition prevents the mixing of differently transforming features, ensuring that all subsequent operations, linear or non-linear, respect the group's symmetry, thereby maintaining equivariance throughout the network.

Intuitively, the tensor products capture interactions between features in a manner akin to multiplication, producing a higher-dimensional representation. Crucially, this new representation is reducible, so we may decompose it into irreps:

$$V \otimes V \cong \bigoplus_k V_k.$$

It is this decomposition that allows the network to project onto individual irreps, achieving non-trivial feature mixing whilst preserving symmetry constraints.

C DATASETS

We present a visualization of a sample trajectory of uracil from three datasets in Figure 7.

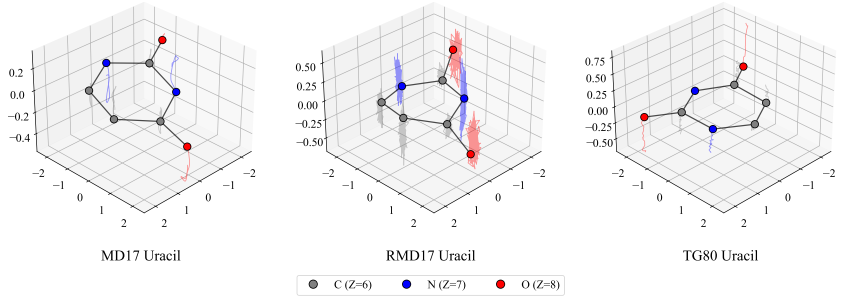

MD17 Uracil

RMD17 Uracil

TG80 Uracil

Figure 7: 3000 timesteps of uracil trajectory from MD17, RMD17, and TG80.

C.1 LICENCES

Table 5: Dataset sources and licenses. We release TG80 under the MIT license.

Dataset	Source	License
MD17	`https://www.sgdml.org/`	`CC BY 4.0`
RMD17	`https://archive.materialscloud.org/record/2020.82`	`CC Zero V1.0 Universal`
MD22	`https://www.sgdml.org/`	`CC BY 4.0`
TG80	To be released at `URL`	`MIT`

C.2 MODEL INPUTS AND THE DATALOADER

Our compound representations follow (Shi et al., 2021; Xu et al., 2024). We model hydrogen atoms implicitly and concatenate the position and velocity norms for each node i with their respective vectors. Unlike their implementations, we avoid explicit graph construction and do not include edge labels describing atomic bond geometries.

We duplicate all frames $\mathcal{G}^{(t)} \to \{\mathcal{G}^{(t)}\}^P$ during dataset initialization, producing a five-fold improvement in throughput compared to previous dataloaders in Table 6.

Table 6: Mean time (seconds) to produce 10 000 batches over 100 benchmark runs. Batch size = 100, 500 samples, $\Delta t = 3000$, 500 warmup batches.

	Aspirin	Ethanol	Naphthalene	Toluene
EGNO	0.060±0.024	0.024±0.016	0.056±0.024	0.039±0.024
ATOM	**0.005**±0.002	**0.007**±0.002	**0.008**±0.004	**0.006**±0.002

C.3 NUMERICAL STABILITY

We evaluate the numerical stability of MD17, RMD17, and TG80. MD17 benzene exhibits substantial center-of-mass drift in Figure 8a, which is also partially visible in the consistent motion trails shown in Figure 11a. RMD17 exhibits improved stability, with no center-of-mass drift exceeding 1×10^4. TG80 shows the lowest drift of all datasets, and expectedly includes more molecules with high per-step drift (due to more complex sterically hindered geometries).

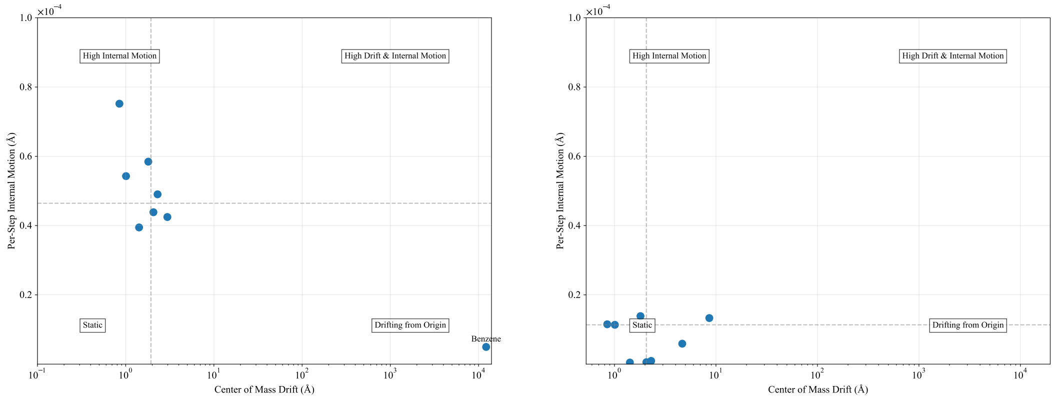

(a) MD17 molecules are largely consistent, except for benzene, which exhibits substantial drift.

(b) RMD17 molecules are more numerically stable, supporting their use in future benchmarks.

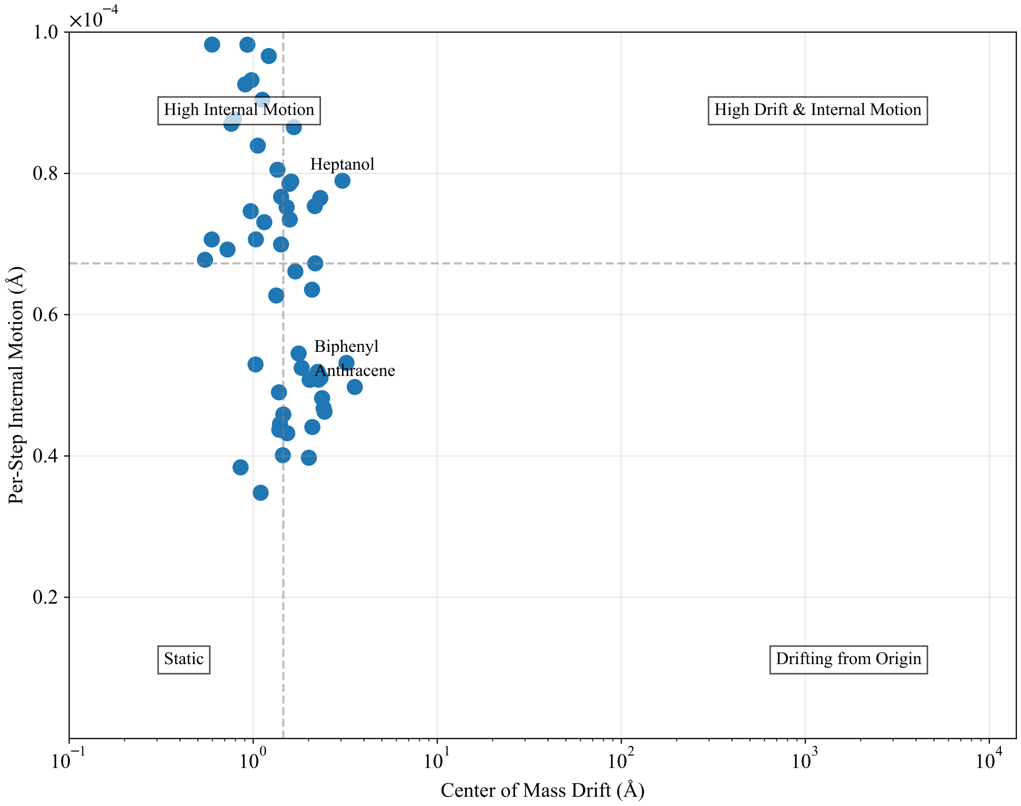

(c) TG80 dataset exhibits the lowest centre-of-mass drift among the evaluated MD datasets.

Figure 8: Comparison of numerical stability across MD17, RMD17, and TG80 datasets. Dashed lines denote the mean centre-of-mass drift and per-step motion; datapoints exceeding two standard deviations are annotated.

C.4 TG80 GENERATION ALGORITHM

We first recall the definition of Tanimoto T similarity between two bit vectors X, Y as

$$\mathrm{T}(X, Y) = \frac{|X \cap Y|}{|X \cup Y|},$$

which is identical to the definition of the Jaccard similarity in this case (Rogers & Tanimoto, 1960).

To generate TG80, we randomly shuffled the PubChem dataset, then iterated through all compounds until 40 were found that matched the following criteria:

1. Simplified Molecular-input Line-entry System (SMILES) encode a valid molecular structure
2. No more heavy atoms than the corresponding seed molecule
3. Only contain {C, H, O, N} atoms
4. No more than five oxygen atoms
5. No more than three nitrogen atoms
6. No disconnected molecular fragments (e.g., salts)
7. Tanimoto similarity to at least one seed molecule greater than 0.875, less than 0.925
8. Tanimoto similarity to a previously selected molecule is no more than 0.2

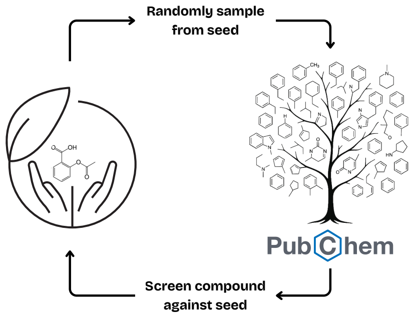

Figure 9: Construction of TG80 from an initial seed using the PubChem database.

This controlled selection procedure generates structurally analogous subsets around each seed molecule whilst preventing convergence to highly similar molecules across different seed groups.

Only 2,488 of the 173 million in the PubChem library satisfied the filtration criteria above. This low yield largely reflects the cumulative effect of criterion 8: as more molecules are added, it becomes harder to find candidates sufficiently dissimilar to all prior selections. Given that the average Tanimoto similarity to our seed set was just 0.1492, the 0.875 threshold was highly selective. Dataset generation code is available at ANONYMIZED.

C.5 MOLECULAR DYNAMICS SIMULATIONS

We present a complete overview of the DFT parameters used to generate MD17 (Chmiela et al., 2017), RMD17 (Christensen & von Lilienfeld, 2020), MD22 (Chmiela et al., 2023), and TG80.

Table 7: An overview of the methodologies used to generate the MD datasets featured.

	DFT Functional	Dispersion Corrections	Basis set	Timestep	Temperature
MD17	PBE	TS	NAO	0.5 fs	500K
RMD17	PBE	None	def2-SVP	0.5 fs	500K
MD22	PBE	MBD	NAO	1.0 fs	500K
TG80	PBE	Δ4	def2-SVP	1.0 fs	300K

D ARCHITECTURAL DETAILS

D.1 FULLY EQUIVARIANT ATOM

To achieve the full equivariance discussed in Figure 5, we employ a canonicalization network approach, which removes Euclidean gauge before learning and then reinstates it afterwards (Kaba et al., 2023). This preserves equivariance of the whole network, even with the use of non-equivariant architectures in the trunk.

We first make data translation equivalent by centering

$$\mu = \frac{1}{N}\sum_{i=1}^{N} x_i, \qquad \bar{x}_i = x_i - \mu. \tag{2}$$

We then remove rotations by aligning to the second moment

$$S = \tfrac{1}{N}\sum_{i=1}^{N} \bar{x}_i \bar{x}_i^\top = \sum_{k=1}^{3} \lambda_k e_k e_k^\top \quad (\lambda_1 \geq \lambda_2 \geq \lambda_3), \tag{3}$$

and choose e_1 as the principal axis and orthonormalise

$$e_2 \leftarrow \frac{e_2 - (e_2^\top e_1)e_1}{\|e_2 - (e_2^\top e_1)e_1\|}, \qquad e_3 = e_1 \times e_2. \tag{4}$$

We can then form $Q = [e_1, e_2, e_3] \in \mathrm{SO}(3)$ and canonicalise

$$\tilde{x}_i = (x_i - \mu)\, Q, \qquad \tilde{v}_i = v_i\, Q. \tag{5}$$

We fix the eigenvector sign ambiguity using the chirality pseudoscalar $c_0 = \sum_{i=1}^{N} x_i \times v_i$ at the reference time (flip e_1 to satisfy $e_1^\top c_0 \geq 0$, then adjust e_2, e_3 jointly to keep right-handedness). Let F be an arbitrary trunk acting in the canonical frame; with per-atom canonical outputs $\hat{y}_i = F(\{\tilde{x}_j, \tilde{v}_j\}_{j=1}^{N})_i$, we decanonicalise by

$$y_i = \hat{y}_i\, Q^\top + \mu. \tag{6}$$

This results in exact $\mathrm{SE}(3)$-equivariance (Kaba et al., 2023) and permits non-equivariant trunks.

D.2 RANDOM-WALK POSITIONAL ENCODINGS

In the multitask case, we add row-normalized random walk positional encoding (RWPE) to equip ATOM and EGNO with multiscale connectivity features, enhancing their ability to distinguish non-isomorphic graphs (Dwivedi et al., 2022; Ma et al., 2023). We first form a ε-neighborhood graph from our pointclouds as:

$$G = (V, E), \quad V = \{i\}, \quad E = \{(i,j) : \|(x,y,z)_i - (x,y,z)_j\|_2 < \varepsilon\}. \tag{7}$$

We set $\varepsilon = 1.6$, as covalent bonds typically range from 1.14 Å to 2.0 Å in length (Lobato et al., 2021) and highlight that this construction does not necessitate prior knowledge of the graph structure.

Let $\mathbf{A} \in \mathbb{R}^{n \times n}$ denote the adjacency matrix of this graph, and let $\mathbf{D} = \mathrm{diag}(\mathbf{A}\mathbf{1})$ represent its degree matrix. We construct the random walk transition matrix as $\mathbf{M} = \mathbf{D}^{-1}\mathbf{A}$ then compute matrix powers of $\mathbf{M}$ up to a maximum walk-length K, defining the self-return probabilities for each node as

$$p_i^{(k)} = \left(\mathbf{M}^k\right)_{ii}, \quad k = 1, \ldots, K. \tag{8}$$

These probabilities are collected into vectors $\mathbf{p}_i \in \mathbb{R}^K$ and concatenated with the phase space to form $\hat{\mathbf{z}} = (\mathbf{v} \,\|\, \mathcal{Z} \,\|\, \mathbf{p}) \in W_{\text{in}}$. Here, the input feature space is redefined as $W_{\text{in}} = V_{\text{in}} \oplus \rho_0^{\text{even}} \oplus \left(\rho_0^{\text{even}} \otimes \mathbb{R}^K\right)$, and the subsequent equivariant maps are modified in kind.

D.3 VALUE-RESIDUAL LEARNING

We employ value-residual learning wherein each transformer block receives the output of the first block via a residual connection to stabilize training and information flow through the network (Zhou et al., 2024b). Inspired by (Jordan, 2024), we add a learned coefficient to weight this residual. Here, v denotes the current block's value output, and v_1 represents the initial block's value. A learnable parameter α is passed through a sigmoid to obtain the weighting coefficient:

$$\lambda = \sigma(\alpha). \tag{9}$$

The combined output is then given by:

$$v = \lambda\, v + (1 - \lambda)\, v_1. \tag{10}$$

In practice, we lock the first block's λ value to 0.5. We report the learned λ values in Figure 10.

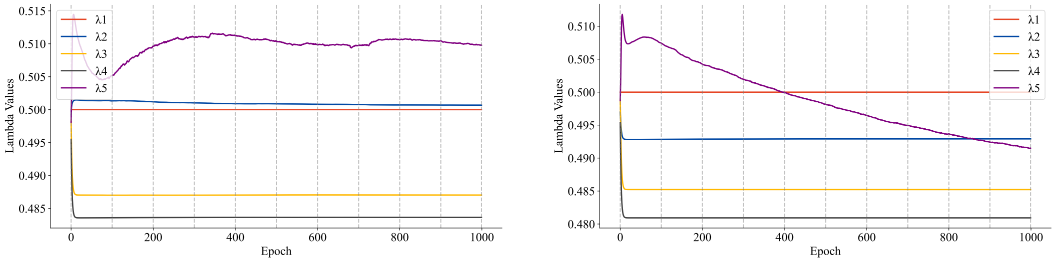

(a) Aspirin

(b) Uracil

Figure 10: Learned value residuals for MD17 training over 1000 epochs.

D.4 DELTA-PREDICTION

When delta-prediction is enabled, as in Figure 5, we incorporate the initial positions $\mathbf{x}$ as a residual term, reformulating the model as an operator that learns a displacement field rather than predicting absolute positions. We express this as:

$$\mathbf{x}^{\dagger} = \text{Project}(\mathbf{x}_{\text{out}}) + \mathbf{x}. \tag{11}$$

Although this approach is implemented in both EGNN and EGNO, we found it was disabled by default in the codebase of the latter (Garcia Satorras et al., 2021; Xu et al., 2024). Based on empirical results from our ablations, Figure 5, we argue there is sufficient evidence to discourage the use of delta-prediction in neural operator-based molecular dynamics simulations.

E FURTHER EXPERIMENTS

We conduct further experiments on single-task and multitask learning. We consider performance under tail discretization and report results on the RMD17 dataset. For multitask learning, we report performance under random cluster assignment and S2S metrics for the experiments in Section 4.2.

E.1 FURTHER SINGLE-TASK LEARNING EXPERIMENTS

MD17 with tail discretization We find the performance of both EGNO and ATOM on MD17 with tail discretization remains similar to the performance under uniform discretization discussed in table 1.

Table 8: EGNO and ATOM with final frame sampling. Upper part: S2S MSE. Lower part: S2T MSE.

	Aspirin	Benzene	Ethanol	Malonaldehyde	Naphthalene	Salicylic	Toluene	Uracil
EGNO	$9.66_{\pm 0.12}$	$39.09_{\pm 2.35}$	$4.57_{\pm 0.01}$	$\mathbf{12.92}_{\pm 0.00}$	$0.39_{\pm 0.00}$	$0.88_{\pm 0.01}$	$10.99_{\pm 0.00}$	$0.60_{\pm 0.00}$
ATOM	$\mathbf{6.38}_{\pm 0.17}$	$\mathbf{39.03}_{\pm 3.32}$	$\mathbf{3.62}_{\pm 0.08}$	$15.26_{\pm 0.65}$	$\mathbf{0.39}_{\pm 0.00}$	$\mathbf{0.83}_{\pm 0.01}$	$\mathbf{5.26}_{\pm 0.79}$	$\mathbf{0.55}_{\pm 0.00}$
Gap	$+33.97\%$	$+0.15\%$	$+20.85\%$	-18.06%	$+1.62\%$	$+4.75\%$	$+52.13\%$	$+9.28\%$
EGNO	$9.66_{\pm 0.11}$	$39.15_{\pm 2.28}$	$4.57_{\pm 0.01}$	$\mathbf{12.92}_{\pm 0.01}$	$0.39_{\pm 0.00}$	$0.88_{\pm 0.01}$	$10.99_{\pm 0.00}$	$0.60_{\pm 0.00}$
ATOM	$\mathbf{6.38}_{\pm 0.17}$	$\mathbf{39.03}_{\pm 3.35}$	$\mathbf{3.63}_{\pm 0.08}$	$15.21_{\pm 0.60}$	$\mathbf{0.38}_{\pm 0.00}$	$\mathbf{0.83}_{\pm 0.01}$	$\mathbf{5.27}_{\pm 0.79}$	$\mathbf{0.55}_{\pm 0.00}$
Gap	$+33.91\%$	$+0.30\%$	$+20.66\%$	-17.71%	$+1.82\%$	$+5.02\%$	$+52.08\%$	$+9.44\%$

Revised MD17 Dataset We reach performance parity with EGNO on RMD17, shown in Table 9.

Table 9: EGNO and ATOM with final frame sampling. Upper part: S2S MSE. Lower part: S2T MSE.

	Azobenzene	Ethanol	Malonaldehyde	Naphthalene	Paracetamol	Salicylic	Toluene	Uracil
EGNO	8.96±0.03	**23.26**±0.01	**40.11**±0.05	1.42±0.00	**28.08**±0.01	1.06±0.01	**28.28**±0.01	0.88±0.00
ATOM	**8.88**±0.05	23.49±0.14	40.29±0.13	**1.36**±0.00	30.12±0.87	**1.03**±0.00	28.56±0.04	**0.86**±0.00
Gap	+0.90%	−0.99%	−0.45%	+3.93%	−7.26%	+3.10%	−0.99%	+1.90%
EGNO	8.51±0.03	**23.61**±0.03	**40.32**±0.08	1.42±0.00	**28.01**±0.02	1.07±0.01	**28.23**±0.00	0.87±0.00
ATOM	**8.38**±0.05	23.90±0.15	40.67±0.17	**1.36**±0.00	30.03±0.78	**1.04**±0.00	28.58±0.05	**0.85**±0.00
Gap	+1.47%	−1.27%	−0.88%	+4.39%	−7.21%	+2.78%	−1.23%	+2.00%

E.2 FURTHER MULTITASK LEARNING EXPERIMENTS

Random-split cross-validation on TG80. For completeness, we report multitask results under compound-level random cross-validation, where compounds are randomly assigned to the train, validation, and test sets. Relative to the more challenging out-of-domain (UMAP-based) split in Table 3, EGNO is comparatively stronger; nevertheless, ATOM maintains a consistent lead across folds, with mean improvements of 24.43% on S2S and 23.93% on S2T.

Table 10: S2S MSE ($\times 10^{-2}$) on TG80 across five UMAP cluster assignments.

		Cluster 1	**Cluster 2**	**Cluster 3**	**Cluster 4**	**Cluster 5**
OOD	EGNO	71.83±0.00	76.92±0.00	68.99±0.00	101.27±0.00	83.20±0.00
	ATOM	**53.93**±0.00	**62.40**±0.00	**49.37**±0.00	**70.75**±0.00	**66.75**±0.00
	Gap	+24.92%	+18.88%	+28.45%	+30.14%	+19.77%

Table 11: S2T MSE ($\times 10^{-2}$) on TG80 across five UMAP cluster assignments.

		Cluster 1	**Cluster 2**	**Cluster 3**	**Cluster 4**	**Cluster 5**
OOD	EGNO	63.23±0.00	64.49±0.00	59.18±0.00	85.87±0.00	69.46±0.00
	ATOM	**46.09**±0.00	**54.47**±0.00	**42.90**±0.00	**55.64**±0.00	**59.55**±0.00
	Gap	+27.10%	+15.54%	+27.51%	+35.21%	+14.28%

Multitask S2S results on TG80 under UMAP cluster cross-validation. The S2S side of the multitask learning results follow closely from their S2T counterparts presented in Section 4.2.

Table 12: S2S MSE ($\times 10^{-2}$) on TG80 across five UMAP cluster assignments.

		Cluster 1	**Cluster 2**	**Cluster 3**	**Cluster 4**	**Cluster 5**
ID	EGNO	51.98±0.81	95.86±0.53	142.51±0.58	155.25±0.67	109.25±0.24
	ATOM	**15.49**±1.04	**26.55**±2.13	**28.74**±2.40	**29.81**±2.72	**26.33**±1.98
	Gap (%)	70.20%	72.30%	79.83%	80.80%	75.90%
OOD	EGNO	52.90±0.72	114.14±13.21	149.99±0.34	163.47±1.00	112.36±1.90
	EGNN-S	52.39±0.40	16512.07±12314.09	149.41±0.94	663.54±865.23	111.08±0.62
	EGNN-R	52.08±0.79	**108.89**±1.60	148.67±0.73	163.27±0.16	109.94±0.31
	ATOM	**41.97**±1.24	127.95±122.67	**74.53**±4.82	**80.95**±1.21	**58.26**±1.68
	Gap (%)	19.41%	−17.50%	49.87%	50.42%	47.01%

Multitask S2S Versus Single Task We evaluate a multitask ATOM model trained on all available trajectories, pooling both ID and OOD clusters, against a single-task ATOM trained separately on each compound. The multitasking model achieves losses comparable to or lower than those of the single-task baselines, despite being trained with the same compute resources.

Table 13: MSE $(\times 10^{-2})$ on full-dataset TG80 ATOM and single-task ATOM. S2S upper, S2T lower.

	Formic Acid
Single-task ATOM	26.40
All-data ATOM	**22.39**
Gap (%)	15.19%
Single-task ATOM	**18.10**
All-data ATOM	18.72
Gap (%)	−3.43%

E.3 Monte Carlo Estimation of Quasi-equivariance

For both the pretrained ATOM and the non-equivariant lifting variant, we estimate the quantity in Section 3.1 by Monte Carlo, drawing N random timesteps x_n and, for each, R random rotations $g_{n,r} \in G$. We approximate

$$\varepsilon \approx \frac{1}{N} \sum_{n=1}^{N} \left\| \frac{1}{R} \sum_{r=1}^{R} \big(f\big(\phi(g_{n,r})(x_n)\big) - \rho(g_{n,r})\big(f(x_n)\big)\big) \right\|_2 .$$

We report our estimates of ε for various ATOM models trained on MD17 single task learning in Table 19. In all cases, ATOM shows a substantially lower equivariance defect, supporting our claim that our quasi-equivariant design achieves a kind of middle-ground in the trade-off between expressiveness and strict equivariance.

Table 14: Estimates of Quasi-equivariance ε via Monte Carlo over 20 rotations and 10 timesteps with 2SD intervals.

	Aspirin	Ethanol	Malonaldehyde	Naphthalene	Salicylic	Toluene	Uracil
Non-equivariant ATOM	120.23±153.71	102.50±45.14	26.94±16.04	37.97±12.65	37.81±20.08	57822.95±42872.97	32.29±35.80
ATOM	**28.34**±25.10	**11.09**±9.64	**9.99**±9.82	**17.09**±13.03	**25.46**±21.47	**2744.07**±3108.52	**28.72**±19.20

E.4 Explicit Hydrogen Representation

We hypothesized that our model's underperformance relative to EGNO in predicting malonaldehyde was due to the omission of explicit hydrogens, which limits its ability to capture electron delocalization effects involving hydroxyl hydrogens. We tested two explicit hydrogen methods:

1. Including all hydrogens with gradients computed for all atoms during training
2. Including all hydrogens but computing gradients only for heavy atoms

Contrary to conventional MD practice, neither method improved heavy-atom test loss.

Table 15: ATOM MD17 S2T MSE with implicit hydrogens (ATOM baseline) and two explicit hydrogen approaches.

	Aspirin	Malonaldehyde
Explicit hydrogens 1	7.48±0.11	15.15±0.22
Explicit hydrogens 2	6.96±0.20	13.52±0.10
Implicit hydrogens	6.52±0.08	13.51±0.10

F EXPERIMENTAL DETAILS

F.1 SOFTWARE AND HARDWARE DETAILS

All experiments were conducted using Python 3.12, NumPy 2.2.1 (Harris et al., 2020), PyTorch 2.5.1 (Paszke et al., 2019), e3nn 0.5.6 (Geiger & Smidt, 2022) and PyTorch Optimizer 3.5.0 (Kim, 2021). We use RDKit 2024.9.6 (Landrum et al., 2025) and PubChemPy 1.0.4 to construct TG80. All single-task training was performed on an NVIDIA RTX 5080 (16 GB) with CUDA 12.4, running on Ubuntu 24.04. We use Ase 3.26.0 (Larsen et al., 2017) and MACE-Torch 0.3.14 (Kovács et al., 2025) in the experiments of Appendix F.3.

F.2 TRAINING TIMES AND COMPUTE REQUIREMENTS

Single-task training time We roughly wall-clock normalised our ATOM and EGNO parameter counts, resulting in respective learnable parameter counts of 754 468 and 335 770.

Table 16: Compute cost of single-task training on all MD17 molecules over 1000 epochs. Both ATOM (335 770 params) and EGNO (754 468 params) are under `torch.compile` on a Titan V.

Model	Metric	Azobenzene	Ethanol	Malonaldehyde	Naphthalene	Paracetamol	Salicylic	Toluene	Uracil
EGNO	Time (mins)	4.09 ± 0.15	3.62 ± 0.42	3.65 ± 0.01	5.01 ± 0.02	9.02 ± 1.22	5.16 ± 0.03	3.93 ± 0.02	4.35 ± 0.04
	Total FLOPS ($\times 10^{12}$)	3681.24	3257.70	3282.09	4513.37	8114.44	4641.50	3539.92	3915.98
	Epochs/min	244.48	276.27	274.22	199.41	110.91	193.90	254.24	229.83
ATOM	Time (mins)	5.81 ± 0.02	5.79 ± 0.06	5.79 ± 0.00	5.86 ± 0.01	5.89 ± 0.02	5.85 ± 0.01	5.81 ± 0.01	5.83 ± 0.02
	Total FLOPS ($\times 10^{12}$)	5226.49	5212.53	5213.50	5271.19	5297.84	5263.76	5224.91	5247.33
	Epochs/min	172.20	172.66	172.63	170.74	169.88	170.98	172.25	171.52
Total FLOPS Reduction (%)		−41.98%	−60.01%	−58.85%	−16.79%	+34.71%	−13.41%	−47.60%	−34.00%

Multitask training time In multitask training on TG80, our upsized ATOM model contained 3 557 840 parameters, compared to 335 770 for EGNO. Despite this, ATOM only trained between 5% and 30% slower than EGNO. This is perhaps unsurprising given the much higher FLOPS-utilization of the transformer architecture upon which ATOM is based.

Table 17: Compute cost of single task training on five TG80 molecules over 1000 epochs. Both ATOM (335 770 params) and EGNO (754 468 params) are under `torch.compile` on a Titan V.

Model		Fold1	Fold2	Fold3	Fold4	Fold5
EGNO	Time (mins)	9.61 ± 1.21	8.56 ± 0.06	9.04 ± 0.11	9.31 ± 0.20	8.98 ± 0.01
	Total FLOPS ($\times 10^{12}$)	8645.66	7703.33	8136.98	8378.06	8084.98
	Epochs/min	104.10	116.83	110.61	107.42	111.32
ATOM	Time (mins)	10.16 ± 0.49	10.55 ± 0.02	11.62 ± 0.41	12.38 ± 0.12	10.39 ± 0.41
	Total FLOPS ($\times 10^{12}$)	9140.57	9497.79	10455.34	11141.73	9355.37
	Epochs/min	98.46	94.76	86.08	80.78	96.20
Total FLOPS Reduction (%)		−5.72%	−23.29%	−28.49%	−32.99%	−15.71%

F.3 INFERENCE TIMES

We compare inference times on MD17 and MD22 across ATOM, the pretrained machine learning interaction potential MACE-OFF24 (Medium) (Kovács et al., 2025), and the classical Lennard-Jones potential (Larsen et al., 2017; Schwerdtfeger & Wales, 2024) and the molecular forcefield. We report inference times in seconds with 2SD intervals. We exclude AMBER results on Uracil as we were unable to run simulations for this molecule (Case et al., 2023).

Table 18: Seconds to produce timestep $\Delta T = 3000$ of each MD17 trajectory at `float32` precision.

		Aspirin	Ethanol	Malonaldehyde	Naphthalene	Salicylic	Toluene	Uracil
$\Delta T = 3000$	MACE-OFF	42.605 ±0.945	39.656 ±0.568	39.782 ±0.141	39.916 ±0.155	39.620 ±0.030	40.271 ±2.851	40.166 ±0.902
	AMBER	37.746 ±0.536	38.512 ±1.243	36.806 ±0.194	38.512 ±1.243	37.621 ±1.412	38.061 ±0.848	–
	Lennard-Jones	2.499 ±0.266	1.604 ±0.208	1.529 ±0.039	2.174 ±0.094	1.981 ±0.011	1.906 ±0.006	1.804 ±0.196
	ATOM	0.849 ±0.926	0.259 ±0.097	0.714 ±0.241	0.467 ±0.149	0.450 ±0.090	0.341 ±0.075	0.373 ±0.076
$\Delta T = 10\,000$	MACE-OFF	143.413 ±3.313	142.569 ±5.584	136.380 ±3.964	140.288 ±9.136	140.103 ±3.398	140.372 ±4.754	141.598 ±1.020
	AMBER	133.900 ±3.815	128.385 ±3.812	121.095 ±0.968	121.607 ±1.195	120.319 ±1.591	120.800 ±0.398	–
	Lennard-Jones	7.797 ±0.369	5.533 ±0.425	5.167 ±0.221	7.453 ±0.376	6.721 ±0.418	6.477 ±0.204	5.921 ±0.522
	ATOM	2.554 ±0.945	1.002 ±0.184	1.634 ±0.200	1.098 ±0.209	1.116 ±0.083	0.964 ±0.185	0.990 ±0.171

Table 19: Seconds to produce timestep $\Delta T = 3000$ of each MD22 trajectory at `float32` precision.

	Ac-Ala3-NHME	DHA	Stachyose
MACE-OFF	44.737 ±4.615	42.042 ±0.720	47.913 ±0.546
Lennard-Jones	4.700 ±0.212	3.790 ±0.246	6.613 ±0.147
ATOM	1.302 ±0.766	0.914 ±0.055	3.075 ±0.080

F.4 ATOM HYPERPARAMETERS

We employ the same dataset splitting and discretization parameters reported in Xu et al. (2024) for the MD17. We set the batch size to 192, use the AdamW-AMSGrad optimizer (Loshchilov & Hutter, 2017) with an ϵ of 1×10^{-10} to avoid instability associated with the small gradients produced by zero-initialised weight matrices in early training (Jordan et al., 2025). During multitask training, we reduce the number of epochs to 250 and employ the Muon optimizer (Jordan et al., 2024; Kim, 2021). We present a complete overview of our hyperparameters in Table 20.

Table 20: Hyperparameters for ATOM. MD17 hyperparameters are shared across all molecules unless otherwise noted.

Module		MD17, RMD17, TG80	TG80 Multitask
Training			
	Batch size	192	192
	Epochs	1000	250
	Max grad norm	1.0	1.0
	Label noise σ	0.1	0.1
	Δt	3000	10 000
	Timesteps P	8	8
	Train/Val/Test	$(500, 3\,000, 3\,000)$	$(6\,500, 13\,000, 13\,000)$
	RWPE length	8	8
Optimiser			
	Optimiser type	AdamW-AMSGrad	Muon
	Learning rate	1×10^{-3}	1×10^{-3}
	β_1, β_2	$0.9, 0.999$	$(0.9, 0.999)$
	Weight decay	1×10^{-5}	1×10^{-5}
	ϵ	1×10^{-10}	1×10^{-5}
Model			
	Embedding dim	128	256
	No. layers	5	6
	No. attention heads	8	8
	No. output heads	1	8
	Attention dropout	0.2	0.2
	RoPE frequency	1000	1000
	MLP layers	2	2
	MLP activation	SwiGLU	SwiGLU
	MLP dropout	0.0	0.0
	Norm type	RMS norm	RMS norm
	Learnable value residuals	True	True

F.5 EGNO HYPERPARAMETERS AND EXPERIMENTAL DETAILS

We generated the EGNO results reported in Table 1 with the same discretization parameters and hyperparameters as used in their experiments. We reduce the number of epochs from 10 000 to 2 500, use a batch size of 192 with the AdamW-AMSGrad optimizer (Loshchilov & Hutter, 2017), and select the best validation loss epoch for testing. In the multitask case, we further reduce the number of epochs to 250 and employ the Muon optimizer (Jordan et al., 2024; Kim, 2021). Complete hyperparameters are displayed in Table 21.

Table 21: Hyperparameter values for EGNO across each benchmark dataset.

Module		MD17, RMD17, TG80	TG80 Multitask
Training			
	Batch size	192	192
	Epochs	2500	250
	Max grad norm	Uncapped	Uncapped
	Label noise σ	0.1	0.1
	Δt	3000	10 000
	Timesteps P	8	8
	Train/Val/Test	$(500, 3\,000, 3\,000)$	$(6\,500, 13\,000, 13\,000)$
	RWPE length	8	8
Optimiser			
	Optimiser type	AdamW-AMSGrad	Muon
	Learning rate	1×10^{-3}	1×10^{-3}
	β_1, β_2	$(0.9, 0.999)$	$(0.9, 0.999)$
	Weight decay	1×10^{-5}	1×10^{-5}
	ϵ	1×10^{-10}	1×10^{-5}
Scheduler			
	Scheduler type	StepLR	StepLR
	Step size	2500	2500
	γ	0.5	0.5
Model			
	Embedding dim	64	64
	No. EGNO layers	5	5
	Temporal convolution activation	LeakyRELU	LeakyRELU
	MLP layers	2	2
	MLP activation	SiLU	SiLU
	MLP dropout	0	0
	Time embedding dim	32	32
	Fourier modes	2	2

G PROPOSITIONS AND PROOFS

G.1 KERNEL INTEGRAL FORM OF CROSS-ATTENTION

Proposition G.1. *The cross-attention is equivalent to a kernel integral operator, i.e.,* $\mathrm{softmax}(\text{T-RoPE}(\mathbf{Q})\,\text{T-RoPE}(\mathbf{K}_i)^\top/\sqrt{d_h})\mathbf{V}_i = \int \kappa_i(\mathbf{z},\mathbf{x})v_i(x)d\mu_N(\mathbf{x})$*, where* κ_i *denotes the kernel induced by softmax function,* $v_i(\mathbf{x})$ *denotes the values as a function of* $\mathbf{x}$*, and* μ_N *denotes the empirical measure supported on* $\{\mathbf{x}_j\}_{j=1}^N$.

Proof of Proposition G.1. Following (Gao et al., 2024) we may view our attention as a kernel integral transform by considering $\mathbf{x}_i$ as being sampled from the continuum domain $\Omega \subset \mathbb{R}^3$ for which we define the empirical measure with support on $\{\mathbf{x}_j\}_{j=1}^N \subset \Omega$:

$$\mu_N(\mathbf{x}) = \frac{1}{N}\sum_{i=1}^{N}\delta_{\mathbf{x}_j}, \qquad \int_\Omega g(\mathbf{x})d\mu_N(\mathbf{x}) = \frac{1}{N}\sum_{j=1}^{N} g(\mathbf{x}_j) \tag{12}$$

where δ is the Dirac delta function "selecting" the values at $\mathbf{x}_j$. Given T-RoPE-rotated query and key maps $\tilde{q}_\theta(\mathbf{z}) = R_{p(\mathbf{z})}q_\theta(\mathbf{z}_j)$, $\tilde{k}_i(\mathbf{x}_j) = R_{p(\mathbf{x}_j)}k_{\theta,i}(\mathbf{x}_j)$ we form the data-dependent kernel for feature F:

$$\kappa_{\theta,i}(\mathbf{z},\mathbf{x}_j) = \frac{\exp\big(\langle\tilde{q}(\mathbf{z}),\, \tilde{k}_i(\mathbf{x}_j)\rangle \,/\, \sqrt{d_h}\big)}{\displaystyle\int_\Omega \exp\big(\langle\tilde{q}(\mathbf{z}_j),\, \tilde{k}_i(\mathbf{x}')\rangle \,/\, \sqrt{d_h}\big)\, d\mu_N(\mathbf{x}')}\,. \tag{13}$$

Thus, for any $F \in \mathcal{F}$ we may represent our cross-attention as the kernel integral operator:

$$\big(\mathcal{K}_{\theta,i}\mathbf{v}_j\big)(\mathbf{z}) = \int_\Omega \kappa_{\theta,i}(\mathbf{z},\mathbf{x})\,\mathbf{v}_i(\mathbf{x})\,\mathrm{d}\mu_N(\mathbf{x}), \qquad \int_\Omega \kappa_{\theta,i}(\mathbf{z},\mathbf{x})\,d\mu_N(\mathbf{x}) = 1, \tag{14}$$

which is row-stochastic under the measure in Equation (12). ☐

We remark that the kernel fails to satisfy global Lipschitz continuity (Delattre et al., 2023), unlike FNO (Li et al., 2021), and certain generalization theorems fail as a result (Le & Dik, 2024).

H TRAJECTORY SAMPLES

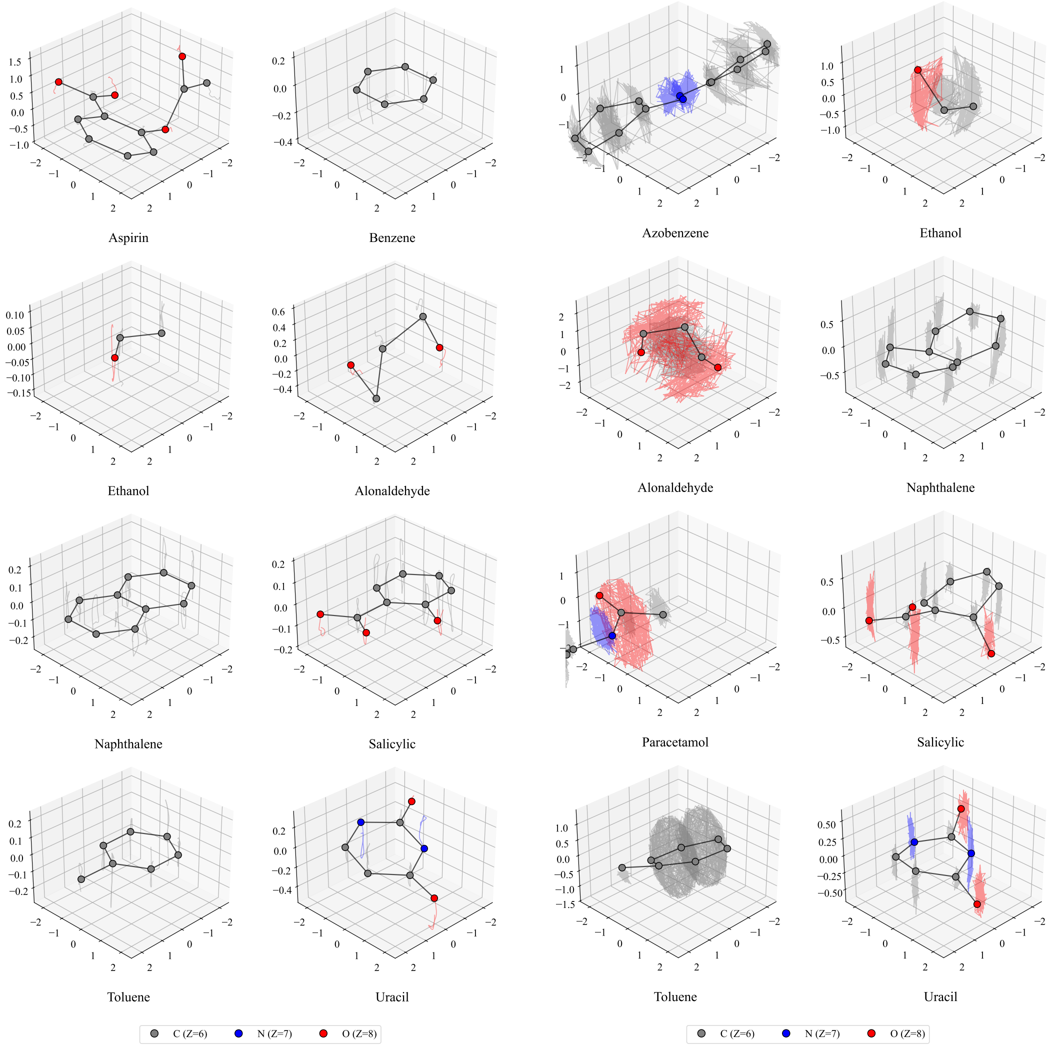

(a) MD17 trajectories (b) RMD17 trajectories

Figure 11: 3000 steps MD trajectories from the MD17 and RMD17 datasets.

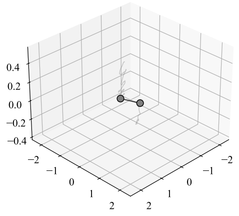

1.2-Dichloroethane

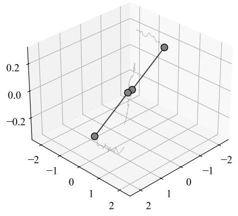

1.3-Butadiene

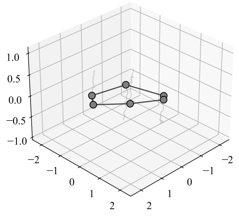

1.3-Cyclohexadiene

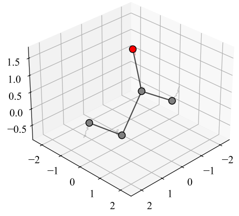

2-Butanone

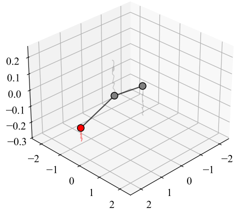

Acetaldehyde

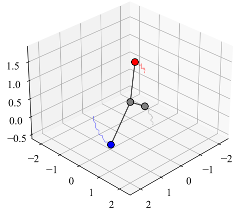

Acetamide

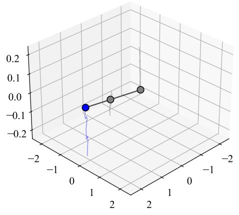

Acetonitrile

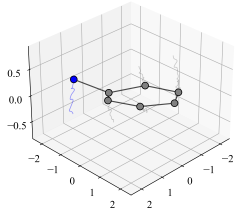

Aniline

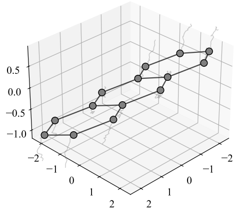

Anthracene

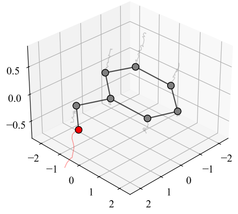

Benzaldehyde

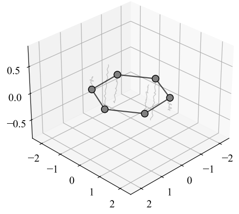

Benzene

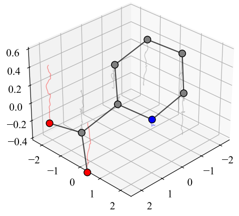

Benzene2

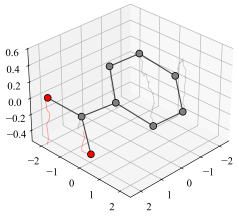

Benzoicacid

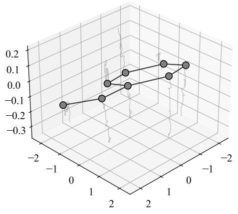

Benzothiophene

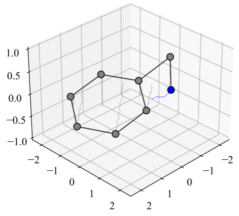

Benzylamine

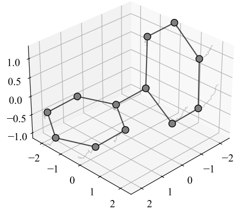

Biphenyl

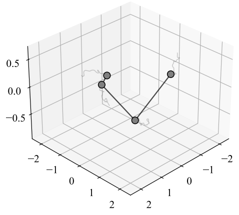

Butane

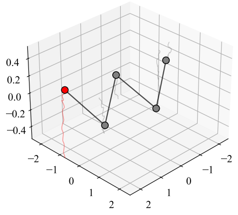

Butanol

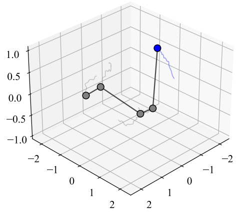

Butylamine

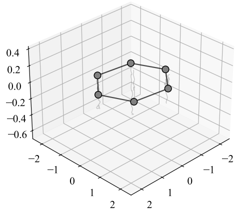

Chlorobenzene

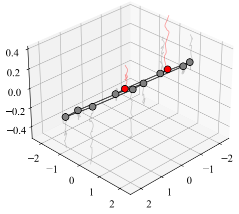

Coumarin

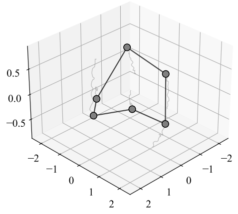

Cyclohexane

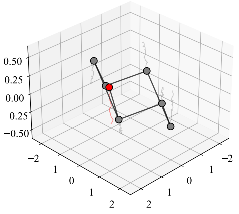

Cyclohexanol

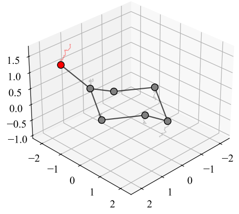

Cyclohexanone

● C (Z=6) ● N (Z=7) ● O (Z=8)

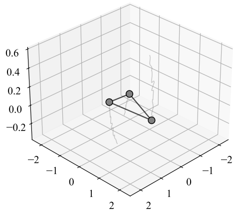

Cyclopropane

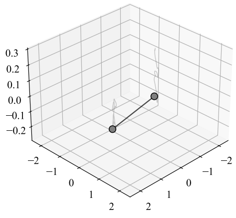

Ethanethiol

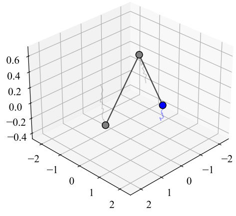

Ethylamine

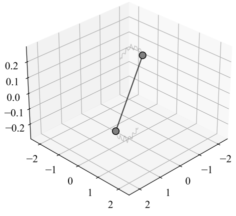

Ethylene

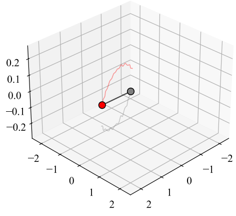

Formaldehyde

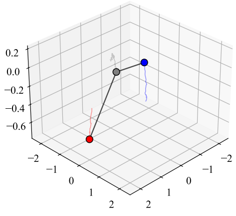

Formamide

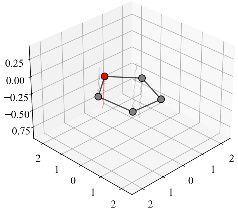

Furan

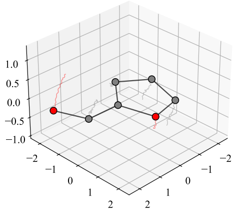

Furfural

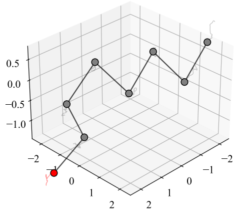

Heptanol

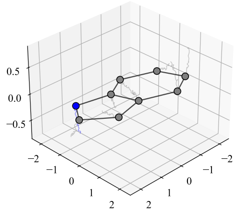

Indole

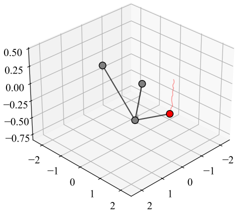

Isopropanol

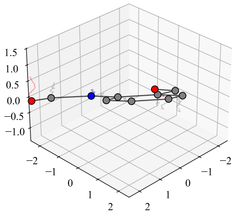

Malondialdehyde1

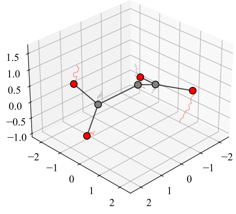

Malonicacid

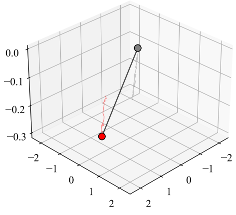

Methanol

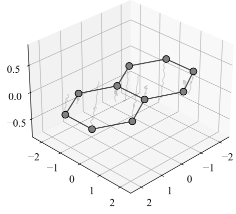

Naphthalene

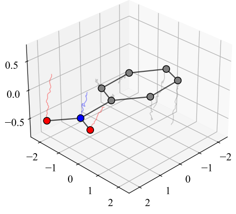

Nitrobenzene

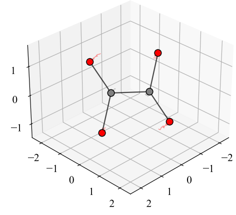

Oxalicacid

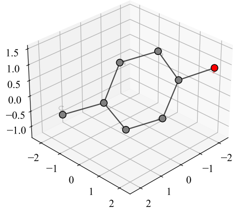

P-Cresol

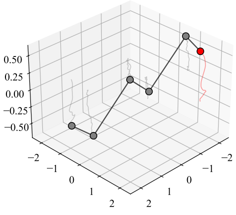

Pentanol

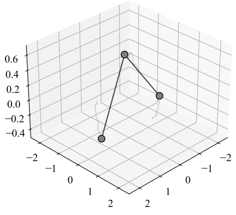

Propane

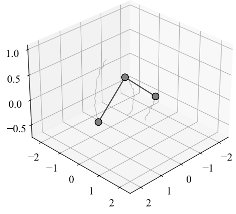

Propylene

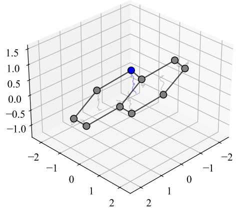

Quinoline

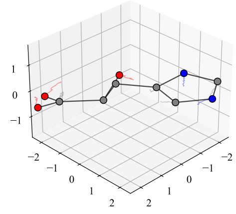

Salicylicacid2

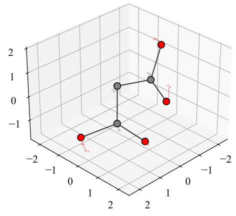

Succinicacid

● C (Z=6) ● N (Z=7) ● O (Z=8)

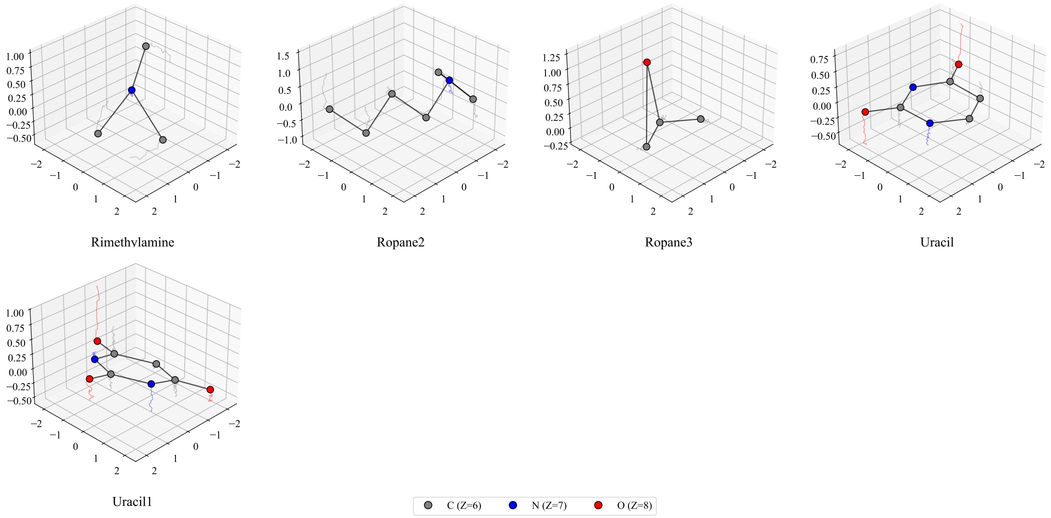

Rimethvlamine

Ropane2

Ropane3

Uracil

Uracil1

Figure 12: 3000-step MD trajectories from TG80. Molecules generated by our dataset expansion algorithm are named according to their seed molecule and the order of their selection.